Deformable Acetabular Implants

an explorative study

Christa de Jonge

April 2019

TUDelft

Deformable Acetabular Implants
an explorative study

By

C.P. de Jonge
4503635

in partial fulfilment of the requirements for the degree of

Master of Science
in Biomedical Engineering

at the Delft University of Technology,
to be defended publicly on 18 April at 15:00.

Supervisor:	H.M.A. Kolken MSc
Thesis committee:	Prof. Dr. Ir. A.A. Zadpoor
	Prof. Dr. Ir. H.H. Weinans

TUDelft

Preface

In 2015 ben ik afgestudeerd aan de Vrije Universiteit van Amsterdam met de master Human Movement Sciences. Op dat moment had ik nog niet het gevoel klaar te zijn voor het werkende leven en wilde ik graag mijn horizon verbreden. Ik ben opgegroeid in Delft, en de technische universiteit om de hoek was altijd interessant voor mij. Na het afronden van de middelbare school heb ik daar geen passende bacheloropleiding kunnen vinden, maar na mijn afstuderen in Amsterdam wekte de master Biomedical Engineering mijn interesse. Zo geschiedde, ik startte met deze master en koos de specialisatie "Tissue Biomechanics and Implants".

Gedurende het eerste jaar van de master heb ik interessante en minder interessante vakken gevolgd. Daarnaast heb ik een leuke tijd gehad als student in "mijn eigen" stad, Delft. In het tweede jaar heb ik een hele leuke en leerzame tijd gehad tijdens mijn stage op de afdeling medische technologie in het Academisch Ziekenhuis in Paramaribo. Wat volgde was mijn afstudeerproject, waarvoor het even zoeken was naar het juiste onderwerp, maar dat heb ik zeker gevonden. Met enthousiasme werd ik geïntroduceerd in het lopende project over vervormbare implantaten. Hiervoor wil ik Amir Zadpoor en Eline Kolken hartelijk bedanken.
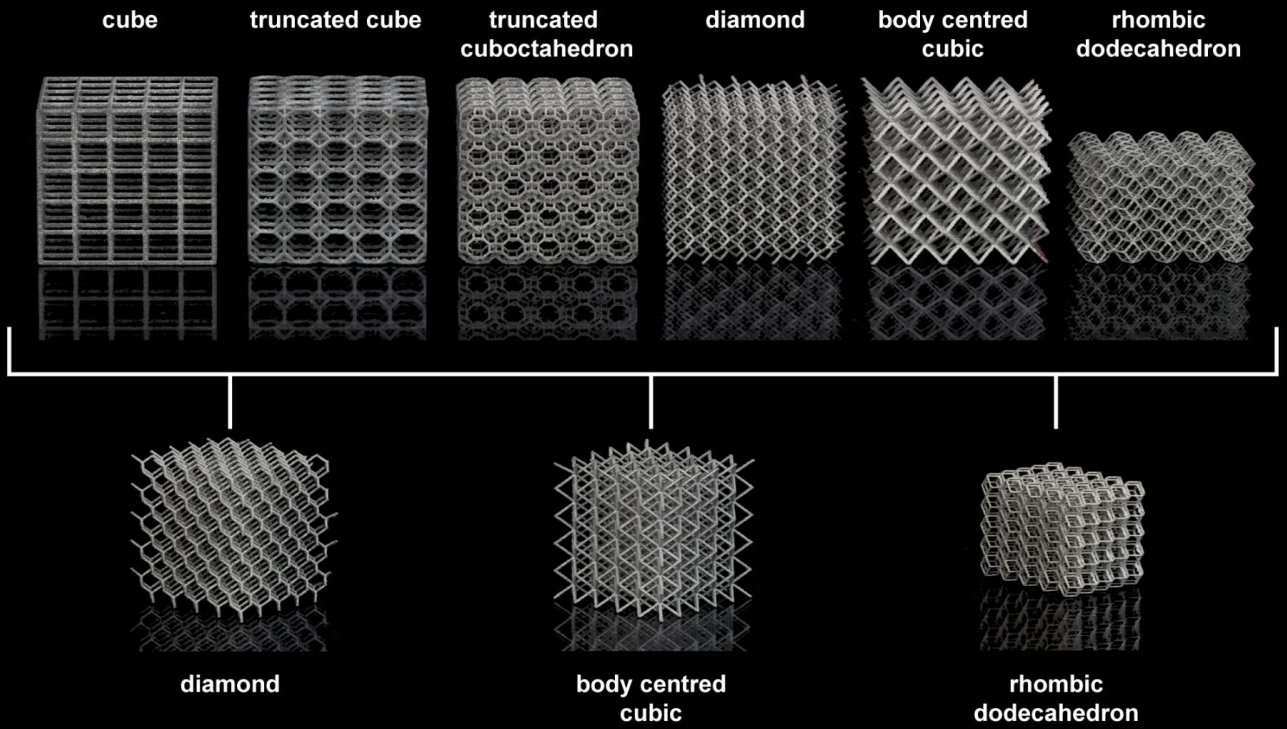
Gedurende mijn project heb ik vanuit verschillende kanten hulp gekregen. Dankzij Tom vander Sloten en Aritz Fontecha van 3D Systems kon ik werken met hele nette samples. Tijdens het testen heb ik mij altijd heel welkom gevoeld in de vliegtuighal van de faculteit Lucht- en Ruimtevaart dankzij Gertjan Mulder, Johan Boender, Berthil Grashof en Misja Huizinga. Verder wil ik Wim Velt en Reinier van Antwerpen bedanken die mij geduldig wegwijs hebben gemaakt in de werkplaats van 3ME. Voor het maken en analyseren van de µCT scans heb ik hulp gekregen van Behdad Pouran. Verder wil ik Sander, Harrie, Alexander, Lennart, Michiel, Joëll, Koen en natuurlijk Amir en Eline bedanken voor onze leerzame en interessante maandelijkse meetings. Eline, jou wil ik in het bijzonder bedanken voor je betrokkenheid bij mijn project. Onze samenwerking vond ik heel prettig. Ik ben er trots op om samen met jou mijn eerste artikel te hebben gepubliceerd.

De echte steun gedurende dit project heb ik natuurlijk gekregen van vrienden en familie. Lieve pap en mam ik ben jullie heel dankbaar dat ik dankzij jullie steun ook mijn tweede master heb kunnen volbrengen. Lieve Gijs, bedankt voor de heerlijke koffietjes en kletspraatjes. Dankzij de lekkere lunchrondjes met de Nordic Stalkers en koffietjes met Marike heb ik mijn project (bijna) iedere dag even kunnen loslaten. Mijn liefste vriendinnetjes en teamgenootjes van dames 3 wil ik bedanken voor de gezellige momenten die mijn aandacht even van het project afhaalden. Mijn allergrootste dank gaat uit naar mijn liefste Charlotte. Je bent mijn grote steun en toeverlaat, dank je wel. Ik kijk er enorm naar uit om lekker op reis te gaan met jou.
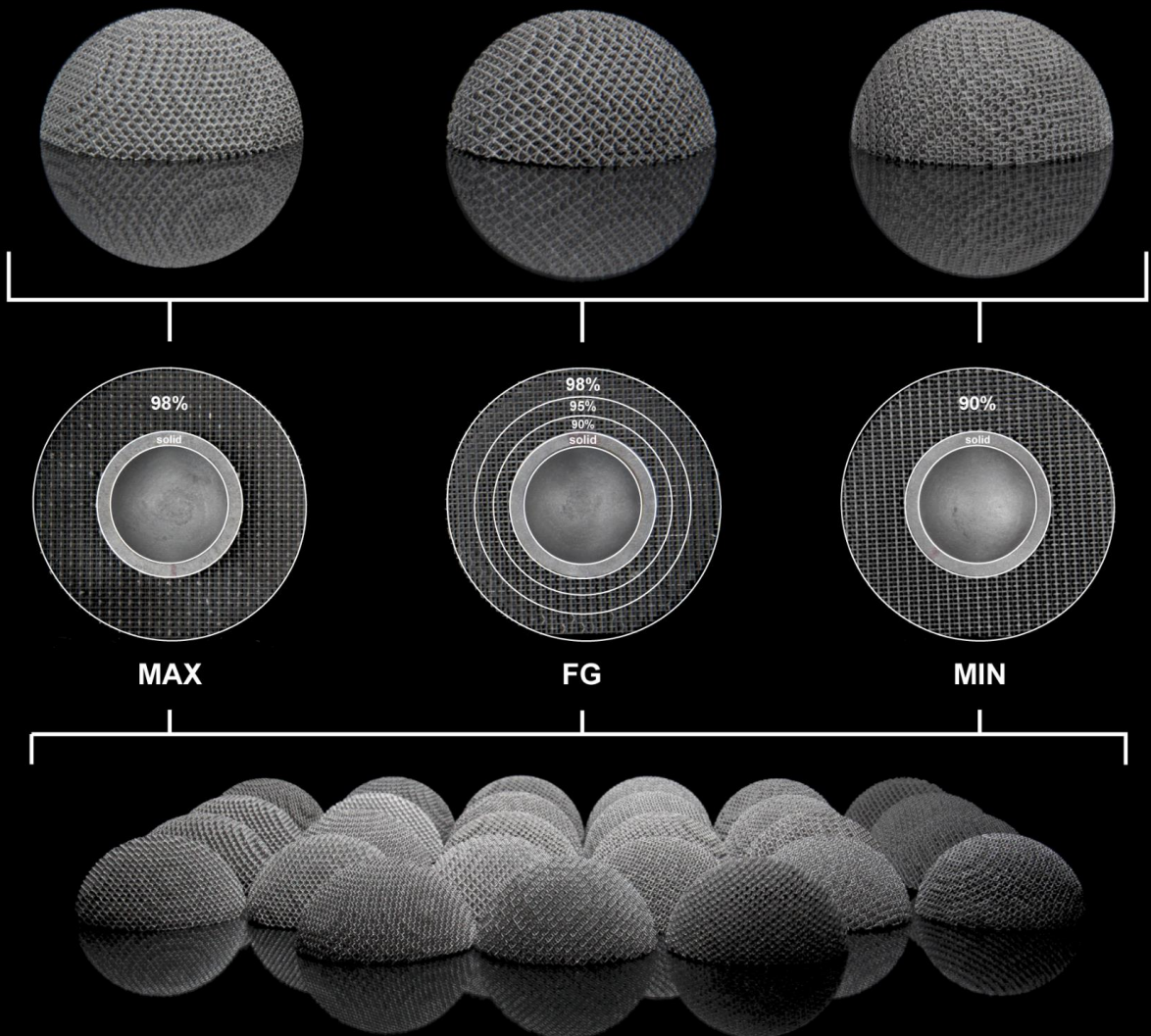
Christa de Jonge
Delft, April 2019

Graphical Abstract

Non-auxetic Meta-biomaterials

cube	truncated cube	truncated cuboctahedron	diamond	body centred cubic	rhombic dodecahedron

diamond

body centred cubic

rhombic dodecahedron

Deformable Acetabular Implants

98%

98%
95%
90%
solid

90%

solid

solid

MAX

FG

MIN

Abstract

An acetabular revision is a very challenging intervention, due to moderate to severe bone deficiencies and poor bone quality. Current solutions for this intervention are associated with inconsistent and unreliable clinical outcomes. This leads to substantial complications, including implant migration and loosening. These complications are, among others, caused by the lack of biological fixation, a non-physiological stress distribution and stress shielding. To encounter these problems a novel concept for an acetabular revision has been presented. The aim of this new design is to plastically deform into massive acetabular bone deficiencies. This will stimulate the surrounding bone and therefore diminishes effect of stress shielding (Wolff's Law). This study explored whether a porous layer made of pure titanium can achieve this space-filling behaviour. The infill of this porous layer is based on meta-biomaterials. The macro-scale properties of this type of materials are determined by their small-scale architecture. The aim of the first part of this study was therefore to systematically study the topology-property relationship of six topological designs, including the cube, truncated cube, truncated cuboctahedron, rhombic dodecahedron, diamond and body centred cubic. These designs were studied by experimentally determining their mechanical properties, including the Poisson's ratio using the Digital Image Correlation (DIC) technique. Afterwards, three topological designs were selected to be implemented in the novel acetabular component, including the diamond, rhombic dodecahedron and body centred cubic. These unit cells showed the lowest stiffness and the highest positive Poisson's ratio over the complete range of concerned porosities (80-98%). Besides, they showed bending-dominated deformation without the failure of struts. The results indicated that these unit cells have the highest capacity to plastically deform as well have the potential of space-filling behaviour. The porosity of the porous layer of the implant functionally graded from very porous at the bone-implant interface to very solid at the joint's articulating surface, which corresponds to bone's hierarchical structure. These implants were compressed inside a bone-mimicking mould, of which the appearance and mechanics resembled an acetabulum with large bone deficiencies. µCT images revealed that the implant based on the diamond unit cell showed the most promising deformability at the mould-implant interface. Although this deformation was promising, the push-in forces needed to compress the implant into the mould were very high (ranging from 3.33 kN to 14.8 kN). Future work is needed to diminish the need for these high push-in forces by making the porous outer layer even more deformable. This novel implant has the potential to increase the biological fixation, preserve the physiological stress distribution and diminish the effect of stress shielding in the acetabular component of a total hip replacement.

Contents

1
Introduction

Total hip arthroplasty (THA) is one of the most clinically successful interventions in healthcare.[1] The demand for THA is expected to increase over the next decades, resulting in an increment of 174% in 2030 with respect to 2005 in the United States.[2] This is mainly caused by population aging as well as the expanded indications for THA in younger and more active patients.[3] Despite the clinical success of the procedure, many people outlive the primary hip implant, leading to 17% of all THA requiring revision.[4] The acetabular component of the THA is involved in more than 50% of the revisions.[5] The main failure modes of this component are loosening (71%), dislocation (16%), migration (6%) and others (7%).[6] An acetabular revision a very challenging intervention, due to moderate to severe bone deficiencies present in the acatabulum.[7]

There are several treatment options available for the revision of an acetabular component, including structural allografts, bone impaction grafting, antiprotrusio cages, (jumbo) non-cemented hemispherical cups, Trabecular Metal augments and shells, oblong cups, cup-cage constructs and custom-made triflange components.[8, 9] None of these procedures is associated with consistent and reliable clinical outcomes.[10, 11] This leads to substantial complication, including implant migration and loosening.[10] These complications are, among others, caused by the lack of biological fixation, a non-physiological stress distribution and stress shielding.[8, 12] Biological fixation is hard to attain due to the significant bone loss. In some cases an implant is combined with flanges which are screwed to the remaining pubis, ilium and ischium to provide extra biological fixation.[8, 10, 11, 13, 14] Attaching these flanches leads to adequate initial stability of the implant, however it also has some drawbacks. Due to these flanches all external loads are distributed to the attachment regions of the flanches, which leads to non-physiologically load distribution. Additionally, the screws used to attach the flanches are much stiffer than the connecting bone. Due to this, most of the external loads will be carried by the implant, while the surrounding bone will be unloaded. This effect is known as stress-shielding.[12, 15-17] According to Wolff's law lacks unloaded bone the stimulus to remodel itself, which eventually leads to bone resorption.[17-21] This effect should obviously be avoided.

These problems have encouraged us to design a new acetabular implant with a porous outer layer, that will precisely fit into a massive acetabular bone defect after plastic deformation. This means that the surrounding bone will remain stimulated, which prevents bone resorption. The infill of the porous layer of the implant will be based on mechanical metamaterials. The macro-scale properties of this type of materials are determined by their small-scale architecture.[22, 23] Rationally designing this small-scale topology results in uncommon combinations of mechanical properties which are seldom seen in nature.[22, 23] One could think of a combination of high strength and low stiffness, or exceptional values for the Poisson's ratio.[24, 25] Since we are interested in the biomedical application of the metamaterials, one could speak of a special category of metamaterials, also known as meta-biomaterials.[25, 26] Meta-biomaterials offer rare combinations of mechanical (e.g. stiffness, strength), topological (e.g. curvature), mass transport (e.g. permeability, diffusivity) and biological (e.g. tissue regeneration performance) properties.[25] These meta-biomaterials may have bone-mimicking properties which could make them ideal candidates for bone substitutes. Recent advances in additive manufacturing (AM) techniques, including selective laser melting (SLM) and electron beam melting (EBM), have boosted the production of any porous structure, including meta-biomaterials.[27-29] These techniques offer several advantages, such as high precision over the small-scale topology as well as design freedom.[27-29]

This graduation project consists of two parts. In the first part the most favourable small-scale topologies (also known as unit cell designs) for the porous layer of the acetabular implant are determined. Therefore, the relationship between the topological design of meta-biomaterials and their mechanical properties is systematically studied. This relationship is extensively studied for meta-biomaterials based on Ti-6Al-4V.[30] In the current study, the focus will be on structures based on commercially pure titanium (CP-It). This material type has the potential of more ductile behaviour compared to is alloyed counterpart.[31] This ductile behaviour is expected to enhance the deformability of the porous layer of the acetabular implant. The following unit cells are considered: the cube, the truncated cube, the truncated cuboctahedron, the rhombic dodecahedron, the diamond and the body centred cubic. These unit cells are reported to present a positive Poisson's ratio (i.e., non-auxetic behaviour).[30] Compressing a non-auxetic meta-biomaterial will result in a lateral expansion. This means that these unit cells have potential to show space-filling behaviour, which is advantageous in the novel deformable acetabular implant. To our best knowledge this study is the first one to experimentally determine the Poisson's ratio of these unit cells using the Digital Image Correlation (DIC) technique.

In the second part of this study, three of considered unit cell types will be selected, based on their space-filling properties. The most ideal unit cell will show a low stiffness, high positive Poisson's ratio and exhibits a bending-dominated deformation pattern without failing struts. These unit cells

will be implemented in the design of an acetabular implant. This implant will have a porous outer layer, which is proposed to plastically deform in massive acetabular bone defects. This allows for a high rate of biological fixation, without the need for extra flanches. The remaining bone will therefore be loaded in a physiological way. Furthermore, the selected unit cells should meet the mechanical properties of bone, which reduces the stress shielding effect, and therefore prevents bone resorption.[12, 15-17, 21] The porosity of the implant will also provide a high surface area for bone ingrowth. The pore size and interconnectivity of the porous part of the implant are important to provide optimum conditions for new capillary and bone formation.[32, 33] In order to enhance the hierarchical similarity between the implant and the host bone even more, the porous part of the implant is executed with a functionally graded (FG) porosity. Numerous studies have examined the effect of FG materials [34-41], but to our knowledge they have not been implemented in an actual biomedical application. The porosity of the unit cells will vary from very porous at the bone-implant interface to very solid at the joint's articulating surface, which corresponds to bone's hierarchical structure.[42-44]

Thus, the aim of this study is to contribute to the knowledge on the topology-property relationship of pure titanium based non-auxetic meta-biomaterials. It does so by experimentally determining the mechanical properties of these materials, including the Poisson's ratio using DIC. The results provide information to facilitate the selection of the most appropriate biomaterial for an envisioned implant application. Besides, this is also an explorative study to demonstrate the potential of deformable FG materials in a biomedical application. This concept has the potential to increase the biological fixation, preserve the physiological stress distribution and diminish the effect of stress shielding in the acetabular component of a total hip replacement.

2

Materials and Methods

2.1 Design of 3D Lattice Structures

In the following paragraphs the designs of the 3D lattice structures will be described. In the first part of this research this involves porous structures with six different types of repeating unit cells ("Non-auxetic meta-biomaterials"). In the second part some of these unit cells will be used to form an acetabular implant.

2.1.1 Non-auxetic Meta-biomaterials

In the first part of this study the focus will be on the relationship between mechanical behaviour and the small-scale topological design of additively manufactured (AM) non-auxetic meta-biomaterials. It is a well-known fact that the properties of lattices depend on their cell topology, material type and porosity (or relative density).[45-47] The mechanical behaviour of this kind of structures based on titanium alloy (Ti-6Al-4V) have been widely studied in the last ten years using computational, analytical and experimental methods. Recently, a comprehensive review on the results of these studies was published.[30]

Although Ti-6Al-4V shows desired behaviour for load-bearing applications (i.e. high strength to weight ratio), it shows less ductile behaviour.[31] Since the aim of this study is to design a deformable acetabular implant, ductility of the material is an important factor. Therefore, another type of material is introduced, namely commercially pure titanium (CP-Ti). This material type has the potential of more ductile behaviour compared to is alloyed counterpart.[31] Additionally, it was observed that CP-Ti porous structures exhibit continuous deformation, without mechanical failure. [31] These results convinced to use this material type.

The following unit cell types will be studied: the diamond (D), the rhombic dodecahedron (RD), the cube (C), the truncated cube (TC), the truncated cuboctahedron (TCO) and the body centred cubic (BCC). Although most of these unit cells are widely studied[30], the mechanical behaviour of the BCC is relatively unknown. This unit cell type is added because of its expected mechanical behaviour. Some studies show that this unit cells presents low values for stiffness and high positive values for

the Poisson's ratio.[35, 48, 49] These properties indicate high ductile behaviour, which is advantageous for the potential application.[35, 48, 49]

Of each of these six topological designs a 5x5x5 cell array was created with 3DXpert 13.0 (3D Systems, Leuven, Belgium) software. Each unit cell was designed to be close to 5x5x5 mm, resulting in a cube that approached 25x25x25 mm (length x width x height). The rhombic dodecahedron unit cell has a deviating cell length in one direction. Therefore, the resulting cube approached 25x17x17 mm (RD-X) and 17x25x17 mm (RD-YZ), respectively. Each of these six lattice structures was designed in five different porosities, namely the following: 80%, 85%, 90%, 95% and 98%. Different porosities were attained by varying the strut thickness. The struts of the unit cells were circular. Unit cell size remained the same in all porosities. The final designs were exported as .STL files. The exact 3DXpert dimensions can be found in Table A1 (Appendix).

In the following paragraphs the geometries of each of the unit cells will be described.

2.1.1.1 Diamond

The diamond (D) is an isotropic geometry which has fourteen nodes and sixteen equal struts (Figure 1). Each node is connected to four struts which are mutually inclined by the angle $\beta \approx 109.47°$.[50] The size of the connecting nodes is designed with the same diameter as the struts. The nodes N1, N2, N3 and N4 are oriented that they coincide with the vertices of the cubic volume SxSxS. The unit cell size (S) relates to the strut length (L) by the following relationship[51]:

$$S \cdot \sqrt{2} = 4 \cdot L \cdot \sin\left(\frac{\beta}{2}\right) \qquad (1)$$
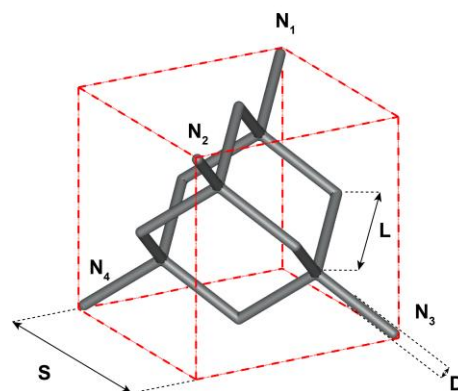

Figure 1: Unit cell design of the diamond, with its corresponding representation of the unit cell size (S), strut length (L), strut diameter (D) and nodes (N).

2.1.1.2 Cube

The cube (C) is a geometry with eight nodes and twelve equal struts (Figure 2). Each node is connected to three struts which are all inclined at a 90° angle. This unit cell is isotropic. Since all struts are aligned with the cubic volume cell, their length (L) is equal to the unit cell size (S).
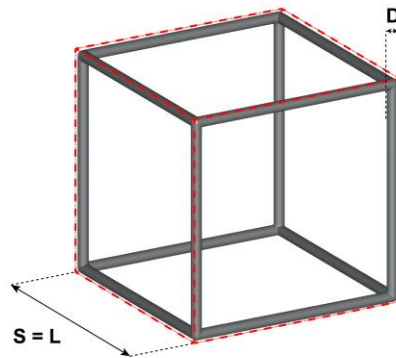

Figure 2: Unit cell design of the cube, with its corresponding representation of the unit cell size (S), strut length (L) and strut diameter (D).

2.1.1.3 Truncated Cube

The truncated cube (TC), also known as the truncated hexahedron, is an Archimedean solid (Figure 3). It is symmetrical in all directions, which means that it is isotropic. The unit cell consists of thirty-six struts, twenty-four nodes, and fourteen regular faces (eight triangular and six octagonal). It has twenty-four inclined and twelve uninclined (i.e. vertical or horizontal) struts.[52] The inclined struts have a length L1. The uninclined struts have a length L2 = 2·α·L1, in which α is the angle between to differently oriented struts. The relationship between the unit cell size (S) and L1 assumes the form[51]:

$$S = L_1 \cdot \left(1 + 2 \cdot \cos\left(\frac{\pi}{4}\right)\right) \qquad (2)$$
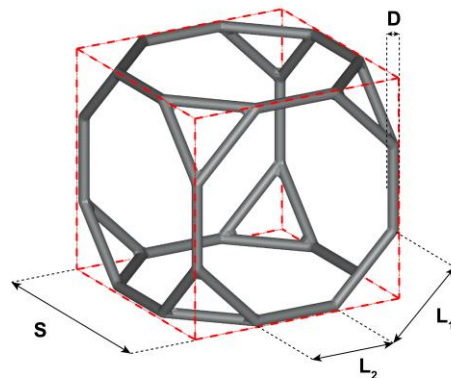

Figure 3: Unit cell design of the truncated cube, with its corresponding representation of the unit cell size (S), strut length (L) and strut diameter (D).

2.1.1.4 Truncated cuboctahedron

The truncated cuboctahedron (TCO), also known as the rhombi cuboctahedron or rhombi truncated cuboctahedron, is an isotropic geometry (Figure 4). This unit cell is an Archimedean solid which has seventy-two struts of equal length (L) which are connected through forty-eight nodes resulting in six octagonal, eight regular hexagonal, and twelve square shaped faces.[53] The strut length (L) relates to the length of the unit cell size (S) via the following equation[51]:

$$S = L \cdot \left(1 + 4 \cdot \cos\left(\frac{\pi}{4}\right)\right) \quad (3)$$
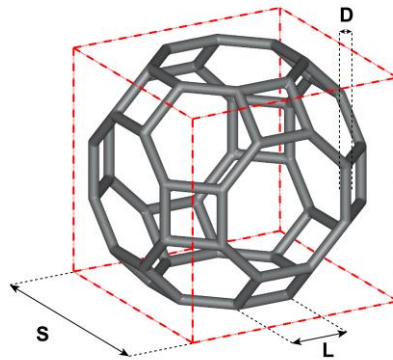

Figure 4: Unit cell design of the truncated cuboctahedron, with its corresponding representation of the unit cell size (S), strut length (L) and strut diameter (D).

2.1.1.5 Rhombic Dodecahedron

The rhombic dodecahedron (RD) has twenty-four equal struts connected by fourteen nodes, resulting in twelve identical rhombic faces (Figure 5).[54] Each rhombus has angles of $2\alpha \approx 70.53°$ and $2\theta \approx 109.47.$[54] The length of the cubic volume side (S) is not equal in all directions. Two directions are equal, and will be denoted as S_{xy}, while the third direction will be denoted as S_z. The relationship between both the unit cell size (S) and the strut length (L) is as follows[54]:

$$S_{xy} = \frac{8 \cdot \sqrt{2}}{\sqrt{3}} \cdot L \quad (4) \qquad\qquad S_z = \frac{12}{\sqrt{3}} \cdot L \quad (5)$$

The RD shows transversely isotropic behaviour. This means its properties are different in one of its directions (X) compared to the other two (Y and Z).[54-56] Therefore the properties in both directions were evaluated. They will be referred to as RD-X and RD-YZ in the remainder of this thesis.
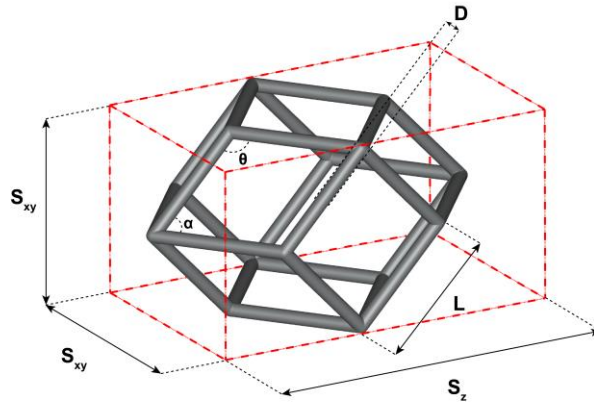
Figure 5: Unit cell design of the rhombic dodecahedron, with its corresponding representation of the unit cell size (S), strut length (L) and strut diameter (D) and angles (α and θ). In this figure the unit cell is oriented in the RD-YZ direction.

2.1.1.6 Body Centred Cubic

The body centred cubic (BCC) is an isotropic unit cell (Figure 6). This geometry has eight struts of equal length (L) and nine nodes. Each strut creates an angle of 45° with its neighbouring strut. The strut length (L) is related to the unit cell size (S) by:

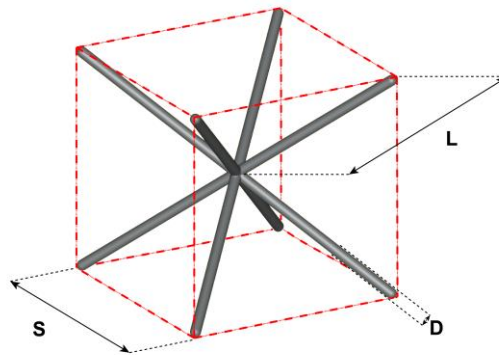$$S = \frac{2 \cdot L}{\sqrt{3}} \qquad (6)$$

Figure 6: Unit cell design of the body centred cubic, with its corresponding representation of the unit cell size (S), strut length (L) and strut diameter (D).

2.1.2 Acetabular Implants

One of the biomedical applications that potentially could benefit from the mechanical properties of the non-auxetic meta-biomaterials is an acetabular component which addresses large bone defects. Currently, there are several treatment options for this kind of deficiencies, including structural allografts, bone impaction grafting, antiporters cages, (jumbo) non-cemented hemispherical cups, oblong cups, cup-cage constructs, Trabecular Metal augments and shells and custom-made triflange components.[8, 9] None of these options shows convincing clinical results.[10, 11] Most common complications are the lack of biological fixation, stress shielding due to a mechanical mismatch

14

between implant and the host bone and a non-physiological stress distribution.[9] In order to overcome these problems a new type of acetabular component design is proposed. This component will have a highly porous outer layer. This layer is intended to plastically deform into the massive acetabular bone defects leading to a high contact area between the implant and the host bone. As a result all surrounding bone will be loaded, which will stimulate the bone to remodel itself in order to prevent bone resorption (Wolffs's Law).[17-21] Furthermore, the mechanical properties of the porous outer layer are designed to be similar to the properties of the surrounding bone. This will lead to a diminished stress shielding effect which prevents bone absorption.[12, 15-17] This porous outer layer will gradually change in porosity, to enhance the hierarchical similarity between the implant and the host bone.[42-44]

To prove this concept, an acetabular implant with a solid inner layer and a thick porous outer layer was designed using Materialise 3-Matic (Materialise, Leuven, Belgium) software. For this porous outer layer the following unit cells were chosen: the diamond, the body centred cubic and the rhombic dodecahedron. These three unit cell types were selected based on a relatively high Poisson's ratio and low elastic gradient found in the first part of this study (See results section). The size of each unit cell was 3x3x3 mm, which is smaller than the size of the unit cells tested in the non-auxetic meta-biomaterials (5x5x5 mm). This way, more layers of unit cells could be incorporated in the 13.75 mm thick outer layer. The porous outer layer consists of 4.5 layers of unit cells, which are again divided in three layers from low porosity on the inside to high porosity at the bone-implant interface. The porosity graded from 90% to maximal printable porosity (approximately 98%). In Figure 7 the exact dimensions of the cup are presented. In this figure it can be seen that besides the porosity, the thickness of the layers also increases from inside to outside. The layer with the highest porosity (outside) will be the thickest, to increase the deformability at this part of the implant. This functionally graded cup will be referred to as FG cup in the remainder of this thesis. Besides this design, two uniformly porous acetabular cups were designed as control samples. They are either fully filled with 90% porosity (MIN) or maximal porosity (MAX). In the MAX design the strut thickness was 200 μm, which is the minimal strut thickness due to printing constraints.[57] Due to this is the maximal porosity slightly different between the three unit cells. The maximal porosity of the BCC and D is 98%, while for the RD the maximal porosity is approximately 96%. The MAX design with the RD infill is therefore 96% porous. The porosity of the layers in the FG design followed the order 90%-93%-96% for this unit cell. For all three unit cells (D, RD, BCC) in total three different designs were developed, namely one functionally graded cup (FG) and two uniformly porous cups (MIN and MAX). This results in nine different designs.
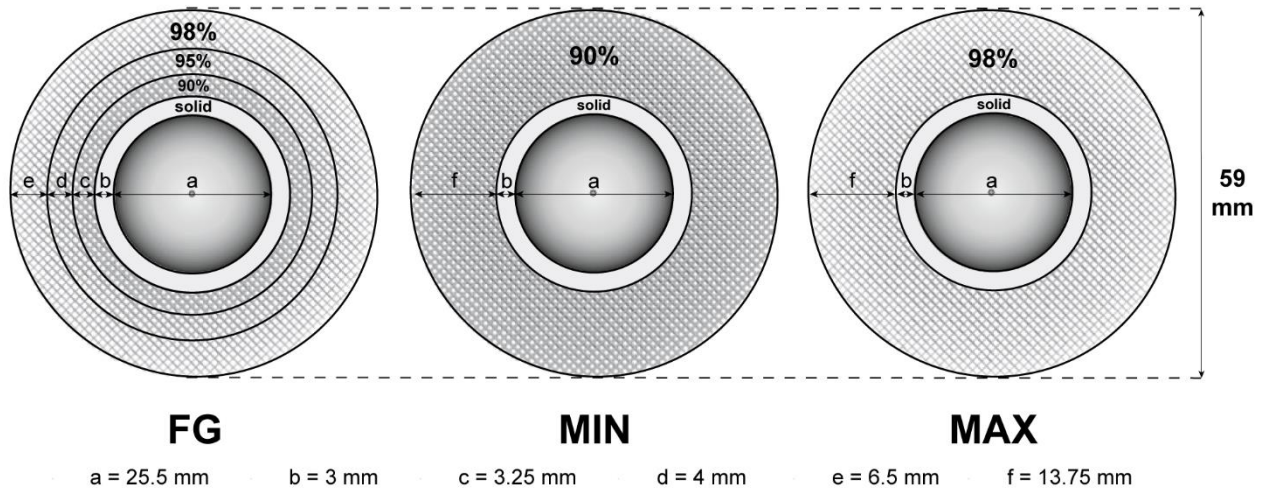
Figure 7: Bottom view of the three different acetabular cup designs with a diamond unit cell infill including the exact dimensions. The designs for the RD unit cell slightly deviated from these dimensions. In this case the maximal printable porosity is 96%. The MAX design is therefore filled with 96% porosity. The porosity of the layers in the FG design followed the order 90%-93%-96% for this unit cell.

2.2 Additive and Subtractive Manufacturing

All designs were fabricated using an additive manufacturing technique called selective laser melting, also known as Direct Metal Printing. To create the test set-up of the acetabular implants, a subtractive manufacturing technique was used. The following paragraphs will describe both techniques.

2.2.1 Selective Laser Melting

Direct Metal Printing (DMP) creates metal parts directly from Computer Aided Designs (CAD), such as .STL files, without the need for tooling. The DMP Software mathematically slices the design in 2D cross-sections, which will act as a blueprint for the DMP equipment. For this project the ProX DMP 320 (3D Systems, Leuven, Belgium) machine was used.[58] A scraper pushes metal powder from the powder supply to create a uniform layer on the base plate. A laser then draws a 2D cross-section on the surface of the build material to fuse the material. Once a single layer is complete, the base plate is lowered by a layer thickness, to make room for the next layer. More metal powder is raised from the material supply to create a new uniform layer of powder on the previously sintered layer. The machine continues to sinter the metal particles layer-by-layer, using a bottom-up approach.[59] This technique has an accuracy up to 200 µm, which means that the strut thickness of the unit cells is limited by this.[57]

Both the non-auxetic meta-biomaterials and the meta-implants are built using commercially pure titanium (CP-Ti) powder.[60] The chemical composition of the material complies with ASTM F67,

ASTM B265, ASTM B348 (grade 1), ISO 5832-2, ISO 13782 and Werkstoff Nr. 3.7025 standards.[61-66] The mechanical properties of the material are presented in Table 1.[60]

After the DMP process is completed, the parts are removed from the build plate using Electrical Discharge Machining (EDM). No additional heat treatment was applied, so the samples are tested as-manufactured. For the non-auxetic meta-biomaterials four specimens per design were printed, resulting in 140 test samples. A total of 27 test samples were fabricated for the acetabular implant, which included three specimens per design.

2.2.2 Subtractive Manufacturing

The acetabular implants were compressed in moulds made of cellular rigid polyurethane foam (20 PCF, #1522-12), acquired from Sawbones (Sawbones Europe AB, Malmö, Sweden). The characteristics of the material (Table 2) are comparable to healthy human cancellous bone, which makes the material suitable to mimic the surrounding acetabular bone.[67] The moulds were cylindrical, with a radius of 40 mm and a height of 80 mm. At one side, a semi-hemisphere with a radius of 30 mm was removed. By milling, several holes and grooves were created to mimic a Paprosky Type 2B acetabular bone defect.[68] The holes had a depth ranging from 6 to 8 mm, and a radius of 5 mm or 10 mm. The grooves were created with a depth ranging from 3 to 6 mm and a radius of 6 to 10 mm. The defects in the moulds have been created in such a way that the acetabular implants can deform with a maximum of 17%. This type of defect and the associated percentage was chosen because it is theoretically impossible for the designed implant to deform to such an extent, due to the imposed displacement (5 mm). This means that the implant can deform throughout the complete range of imposed displacement. The resulting mould can be seen in Figure 8.

Table 1 Mechanical properties of CP-Ti.		
Property	**Metric**	
	mean	std.
Young's Modulus [GPa]	105-120	
Ultimate Strength [MPa]	500	30
Yield Strength [MPa]	380	
Elongation at break [%]		
Horizontal direction (XY)	29	5
Vertical direction (Z)	30	5
Density [g/cm³]	4.51	

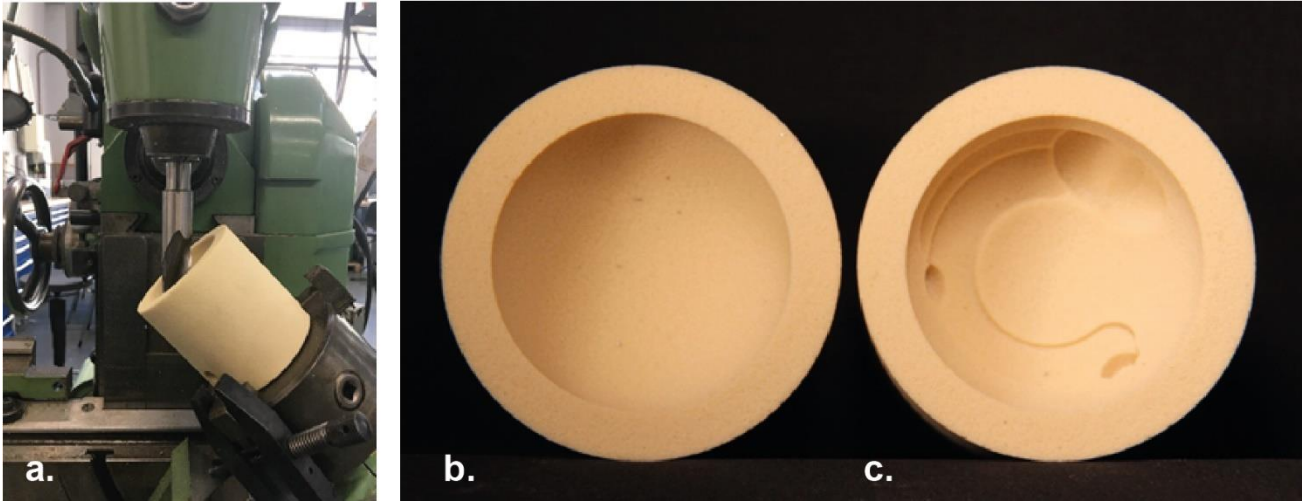| Table 2 Characteristics of the moulds.	
Property	**Metric**
	mean
Density [g/cm³]	0.32
Cell Size [mm]	0.5-1.0
Young's Modulus [MPa]	137
Ultimate Strength [MPa]	5.4

Figure 8: (a) The production of the defects in the moulds. (b) The mould without defects. (c) The mould with defects.

2.3 Morphological Characterization

The morphological features of all AM lattice structures (Figure 9) were characterized using dry weighing. For the acetabular implants, micro-CT (µCT) scans were made to assess their porosity, pore size and strut thickness. The following paragraphs will describe both methods.

2.3.1 Dry Weighing

By using dry weighing, the relative density and subsequently the porosity of the non-auxetic meta-biomaterials and the acetabular implants could be determined. The dimensions of the test specimens were measured to the second decimal place using a calliper. Afterwards all specimens were weighed using an OHAUS Pioneer Balance with an accuracy of 0.1 mg.

2.3.1.1 Non-auxetic Meta-biomaterials

The relative density of the non-auxetic meta-biomaterials is defined as the ratio of the weight of the lattice structure (M_L) to the theoretical weight of a corresponding solid specimen (M_T) assuming a theoretical density of 4.51 g/cm^3 for CP-Ti.[60] In order to determine the relative density of the lattice structure the following equation was used:

$$Relative\ density\ [\%]\ = \frac{M_L}{M_T} \times 100 \quad (7)$$

Subsequently, the porosity is determined as follows:

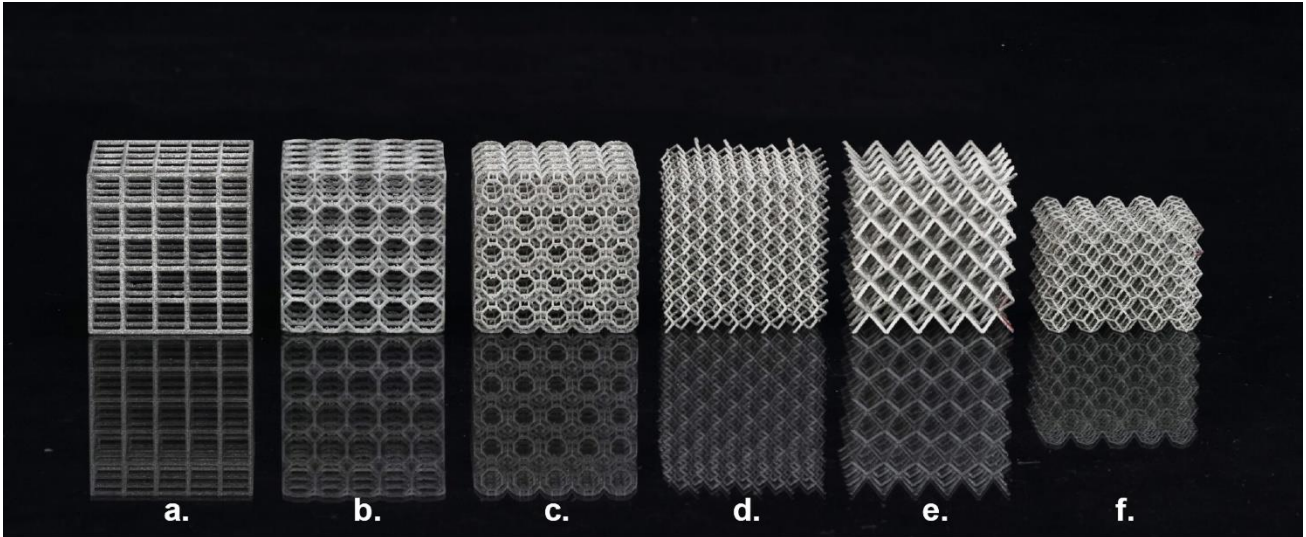$$Porosity\ [\%]\ = 100 - Relative\ density \quad (8)$$

Figure 9: The non-auxetic meta-biomaterials after production. The (a) cube, (b) truncated cube, (c) truncated cuboctahedron, (d) diamond, (e) body centred cubic, (f) rhombic dodecahedron.

2.3.1.1 Acetabular Implants

The relative density of the porous layer of the acetabular implants (Figure 10) has been determined in the same manner as the non-auxetic meta-biomaterials. The mass of the acetabular implants is determined by weighing. In order to determine the mass of the porous outer layer, the mass of the solid inner layer is subtracted from the mass of the actual acetabular implant. The solid inner layer has the same dimension in all designs, which means that the mass is also the same (17.29 gram) assuming a theoretical density of 4.51 g/cm^3 for CP-Ti.[60]. Next, the determined mass of the porous outer layer (M_P) is divided by the theoretical weight of a solid layer (M_S) of the same dimensions, again assuming a theoretical density of 4.51 g/cm^3 for CP-Ti.[60] In order to determine the relative density of the acetabular implants the following equation was used:

$$Relative\ density\ [\%] \ = \ \frac{M_P}{M_S} \times 100 \qquad (9)$$

The porosity is calculated in the same manner as for the lattice structures (equation 8). This procedure could only be followed for the acetabular implants with uniform porosity.

2.3.2 Micro-CT

The purpose of using micro-CT (µCT) scans for the acetabular implants was twofold. Firstly, it was used to perform morphological characterization. Secondly, it could determine the degree of deformation after compression. Therefore, the acetabular cups were scanned before and after compression.
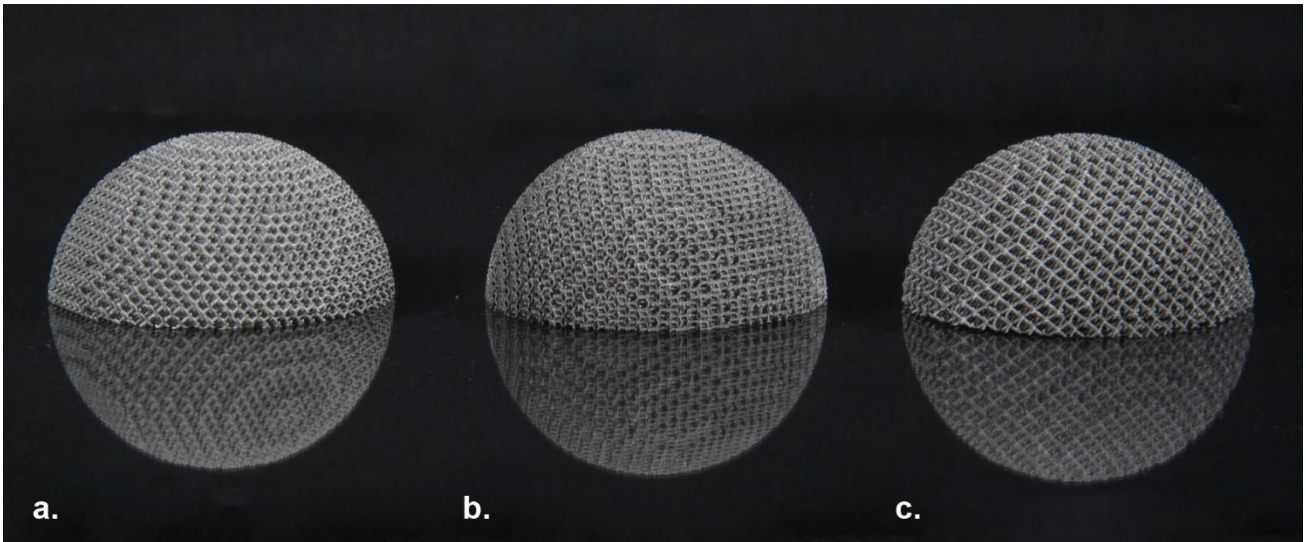
Figure 10: The acetabular implants with the three different unit cell designs at 90% porosity (MIN). Implants based on the (a) diamond, (b) rhombic dodecahedron and (c) body centred cubic.

2.3.2.1 Acetabular Implants

A Quantum FX (Caliper LifeSciences, Alameda, CA) micro CT scanner was used to perform the scans. Tape was used to secure the acetabular cups inside the mould (Figure 11a) during the pre-compression scans. Next, the combined cup and mould was flipped to its side to fit inside a cylindrical sample holder (10 mm in diameter), which was surrounded by a copper filter (Figure 11c). This filter was used to reduce beam hardening effects. The sample holder was placed inside the CT scanner. The scans were performed with a voltage of 90 kV at a current of 200 μA. Scanning time was 120 seconds. Each sample was scanned twice, once with a field of view (FOV) of 60 mm^3 and once with a field of view of 40 mm^3, using the same scanning parameters. In the largest FOV, the complete sample was visible, which resulted in an overview image. The smaller FOV was used to determine the morphological properties, since this FOV had a better resolution compared to the larger FOV.
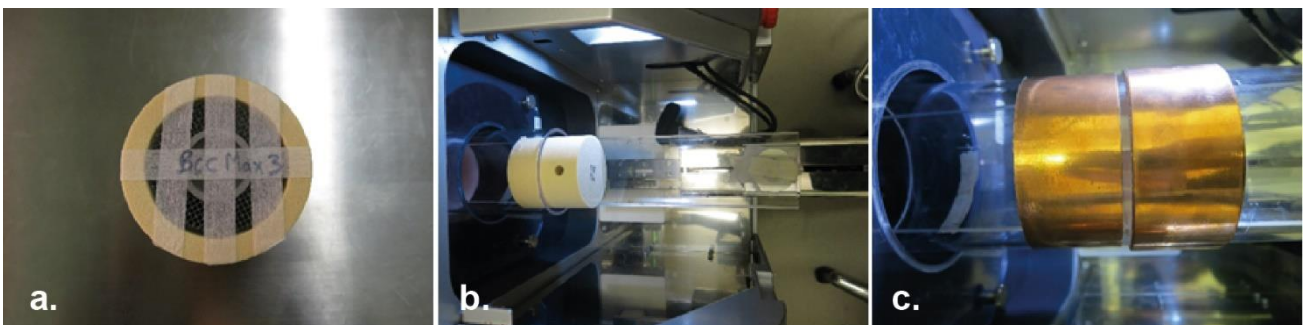

Figure 11: The procedure followed for the μCT scans. (a) The sample are taped inside the mould. (b) The sample and mould are flipped on its side on a cylindrical sample holder, which was surrounded by a copper filter (c).

The acquired 3D images were automatically reconstructed using the built-in software of the micro-CT scanner. Subsequently, the images were transferred to Caliper Analyze 11.0 to obtain 2D slices of the 3D images. These slices were then imported and processed in the software package ImageJ v1.53j (https://imagej.nih.gov/ij/). All images were processed in the following manner. Firstly, the histograms were equalized by cutting off all values above 18000. Then the 2D slices (16-bit images) were transformed to 8-bit images. Subsequently, the scans were thresholded at a threshold limit of 70. Next, an automatic local threshold (Bernsen, radius 15) was applied to create binary images. From this binary image a region of interest (ROI) was selected (equal size for all scans), for which the strut thickness, pore size and overall porosity were determined. This was done using the volume fraction and thickness algorithms available in the BoneJ plugin.[69] Additionally, a 3D reconstruction of the scans was created, using the 3D viewer plugin. Here it was possible to determine the locations of the deformation of the acetabular cups inside the moulds.

The deformation of the porous titanium layer is visually determined by the µCT scans. Additionally, the deformation is also quantitatively evaluated by determining the degree of anisotropy (DA). This value estimates how highly oriented substructures are within a volume, using the mean intercept length technique.[69] The DA was assessed using the anisotropy algorithm of the BoneJ plugin.[69] Default settings of this plugin were used, except for the maximal spheres and tolerance, which were adjusted to 20000 and 0.0005, respectively. Once the tolerance parameter, which is a coefficient of variation, is reached, the anisotropy determination stops. The maximal spheres parameter determines the number of spheres which will be used during anisotropy determination. The obtained value ranges from 0 to 1, from isotropic to anisotropic structures.[69]

The material of the mould is omitted in the scans. After compression, the moulds were cut through to get an idea to which extent they were affected by the compression.

2.4 Mechanical Testing

Once the samples were manufactured, mechanical tests were performed. The following paragraphs will describe the procedures executed to acquire the mechanical properties of the samples.

2.4.1 Static Compression Testing

2.4.1.1 Non-auxetic Meta-biomaterials

In order to obtain the mechanical properties of the lattice structures a procedure based on ISO 13314:2011 was performed.[70] The lattice structures were placed between the platens of the test machine and compressed with a constant deformation rate of 1 mm/min until ± 40% strain (Figure 12). All samples were tested on a Zwick/Roell (Zwick GmbH & Co. KG, Ulm, Germany) static test machine. The samples with the lowest porosity (80%) and some other samples (C 90%, TC 98%
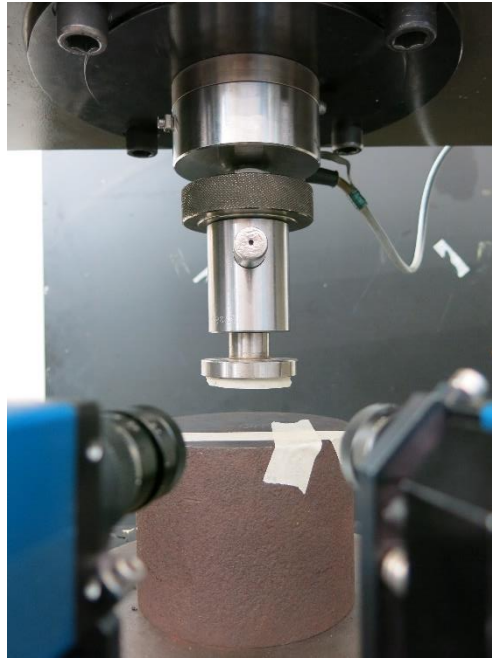
Figure 12: Set-up for the static compression testing of the non-auxetic meta-biomaterials.

and RD-X 85%) were tested on a machine with a 250 kN load cell, all other samples (more porous) were tested on a machine with a 20 kN or 10 kN load cell. Of each design, four specimens were tested.

Based on the static mechanical tests a force-displacement curve was acquired. Based on this information a stress-strain curve is obtained. The stress (σ) is calculated by dividing the applied force (F [N]) by the initial cross-sectional area (A [mm^2]) of the sample perpendicular to the loading direction. The strain (ϵ) is defined as the overall compressive displacement divided by the initial height of the test sample. Based on this stress-strain curve the following parameters could be determined[70]:

First maximum compressive strength (σ_{max}): compressive stress corresponding to the first local maximum in the stress-strain curve.

Elastic gradient (E): the gradient determined between 20%-70% of the σ_{max}.

Plateau stress (σ_{pl}): the arithmetical mean of stresses between 20% and 30% compressive strain. This property is only calculated if the stress-strain curve reached a plateau after the σ_{max}. This value indicates the whether the structures shows the stress that a porous structure can withstand in the plastic region.

2.4.1.2 Acetabular Implants

In order to test the deformability of the acetabular implants, compression tests were performed (Figure 13a). All samples were tested on a Zwick/Roell (Zwick GmbH & Co. KG, Ulm, Germany)

static test machine with a 20 kN load cell. Firstly, the mould was placed on the bottom plate of the static test machine. Subsequently, the acetabular implant was placed inside the mould, using a level to make sure that they were horizontally fitted. To test this system, a steel ball with a diameter of 25 mm, which precisely fitted into the solid inner hemisphere of the acetabular cup, was attached to the load cell using a screw. Tests were performed with a constant deformation rate of 0.5 mm/min until 5 mm deformation. Of each design three specimens were tested.

Based on the static mechanical tests, a force-displacement curve was acquired.

2.4.1.3 Machine Compliance

After the compression tests of both the non-auxetic metamaterials and the acetabular implants, an extra test was preformed to determine the machine compliance. Correction for this factor is an important step in analysing the obtained data.[71] Due to the fairly small deformation measured in this study it is not possible to use extensometers, which is a more conventional method to make up for machine compliance.[71]

Machine compliance was measured by determining the load-displacement relationship without any sample between the compression plates (Figure 13b). A constant deformation rate of 1 mm/min was applied, while recording the resulting load until the maximal allowed load was reached. This test was repeated five times to overcome the effect of hysteresis. Subsequently, a sixth order polynomial was fitted to the mean of the load-displacement relationships. Next, the recorded data in the mechanical tests of the samples was corrected for the measured machine compliance.

2.4.2 Digital Image Correlation

During the axial compression of the non-auxetic meta-biomaterials, Digital Image Correlation (DIC) was used. In the field of experimental solid mechanics, DIC is an established technique to determine surface deformation. Recently, this technique was introduced into porous structures.[48, 72]
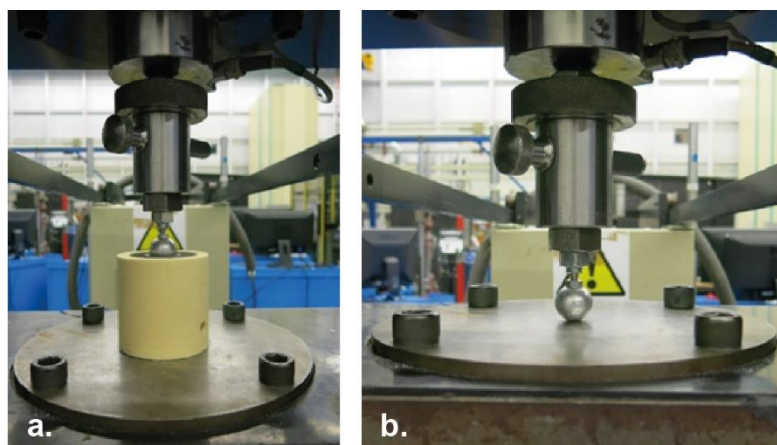

Figure 13: (a) The test set-up of the static compression tests of the acetabular implants. (b) The machine compliance test set-up for the acetabular implant mechanical test set-up

DIC is based on the basic principle of comparing digital pictures of a test specimen at different stages of deformation. By tracking an array of pixels between subsequent images, the surface deformation can be determined. In order to make a distinction between different arrays of pixels, it is important that the pixel pattern is random and unique. In order to obtain such a pixel pattern, surface preparation of the samples is needed. First all lattices were painted black. Next, one side was either painted or stamped white. Subsequently, a black, random speckle pattern was airbrushed on the samples (Figure 14).

Two 4 MP digital cameras (Limess, Krefeld, Germany) were used to capture the sample. The cameras were placed at an angle of approximately 30°. The set up was completed with a light which enhanced the clarity of the image. To calibrate the DIC system several images were taken from a calibration board with 10 x 14-dots (separation of 3 mm). The calibration images were processed by VicSnap software (Correlated Solutions Inc., Irmo, USA). During the compression tests, the samples were captured with a frequency of 1 Hz using VicSnap. The used subset size ranged between 29 and 65 cubic pixels. The step size was kept constant at 7 pixels.

The DIC data were used to determine the Poisson's ratio (v) of the samples. To do that, the images obtained by the two cameras were processed in VIC 3D 8 (Correlated Solutions Inc., Irmo, USA). This software package provides the possibility to obtain the displacement of indicated data points. For each of the lattice structures, an array of 3 by 3 unit cells was selected as the region of interest, which have been presented in Figure 15. By using the data of these points, the strain perpendicular (ε_{xx}) and parallel (ε_{yy}) to the loading direction could be obtained. The Poisson's ratio was calculated in the elastic region of the stress-strain curve with the following equation using MATLAB (2017b):

$$v = -\frac{\varepsilon_{xx}}{\varepsilon_{yy}} \qquad (10)$$
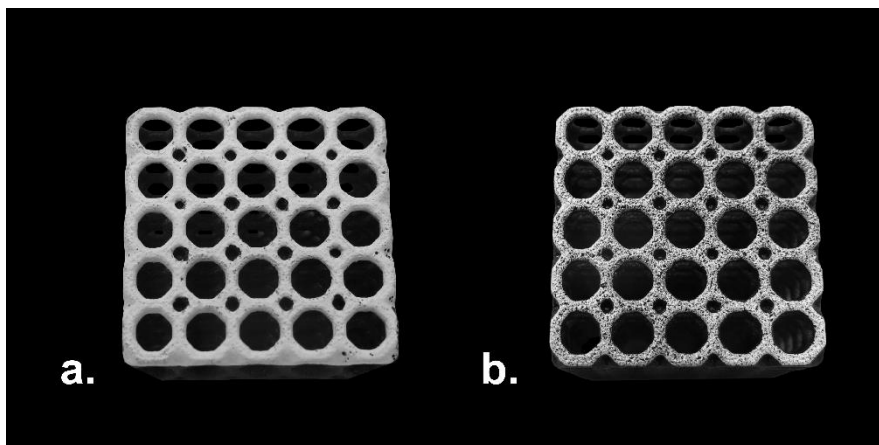

Figure 14: An example of a sample after preparation for DIC. (a) A white painted sample, (b) a sample with a random speckle pattern.
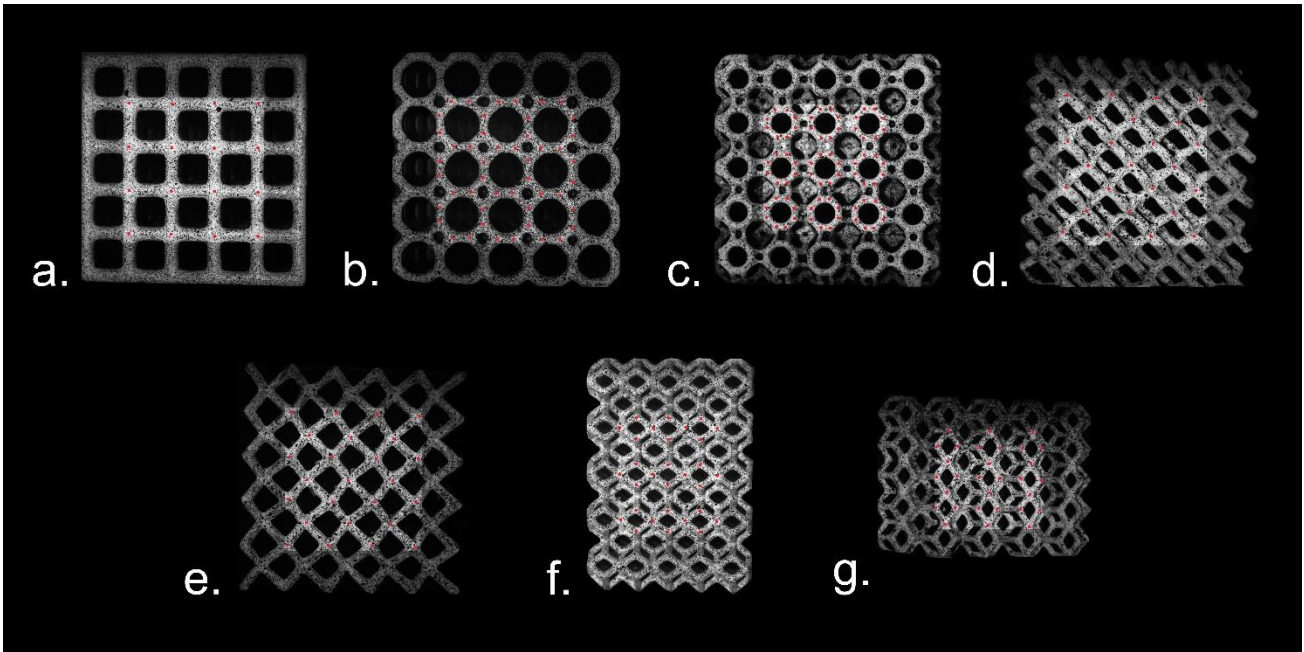
Figure 15: Region of interest selected to determine the Poisson's ratio of the (a) cube, (b) truncated cube, (c) truncated cuboctahedron, (d) diamond, (e) body centred cubic, (f) rhombic dodecahedron (direction X), (g) rhombic dodecahedron (direction YZ)

2.5 Statistical Analysis

The data have been evaluated on their statistical significance using SPSS (IBM, Armonk, NY).[73] Independent and dependent factors were identified to determine which test design had to be selected. There are two independent variables; namely, designed porosity with five levels (80%, 85%, 90%, 95%, 98% porosity), and topological design with seven levels (C, TC, TCO, RD-YZ, RD-X, D and BCC). The dependent variables are first maximum compressive strength, elastic gradient, plateau stress and Poisson's ratio. The two-way ANOVA test design was selected. This test assumes that the data is normally distributed and shows homogeneity of variances. Residual analysis was performed to test both assumptions. Outliers were assessed by inspection of a boxplot; normality was assessed using Shapiro-Wilk's normality test for each of the design and homogeneity of variances was assessed by Levene's test. If the data shows heterogeneity of variance, it might be possible to perform the two-way ANOVA anyway. This is the case when the sample sizes are equal and the ratio of the largest group variance to the smallest group variance is less than 3.[74] Significance is assumed at $p < .05$.

3

Results

3.1 Non-auxetic Meta-biomaterials

3.1.1 Morphological Properties

The morphological properties of the non-auxetic meta-biomaterials have been presented in Table 3. The porosities determined using dry weighing vary between 80.0 – 97.4%. The porosity as-manufactured was slightly higher than the CAD porosity at 80%. For all other porosities the porosity as-manufactured was lower than its designed counterpart. In any case, differences did not exceed 5%. In Figure 16 magnified images of the acetabular implants have been presented.

3.1.2 Mechanical Properties

The mechanical properties of the lattice structures with different unit cell types have been presented in Table 4. The stress-strain curves of the compressive tests of the non-auxetic metamaterials have been presented in Figure 17. Their deformation pattern can be seen in Figure A1 (Appendix). The following paragraphs describe statistical significance of the mechanical properties obtained from the stress-strain curves.
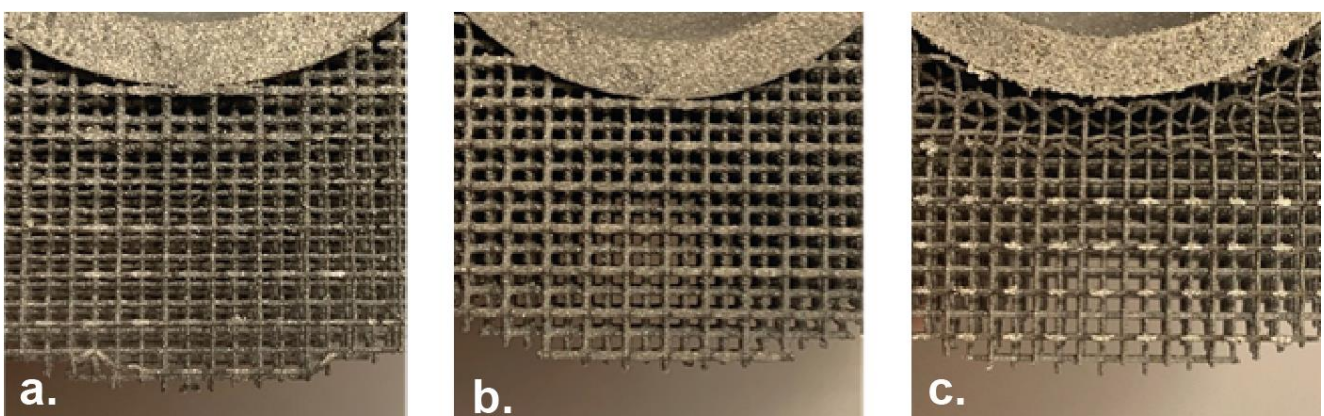

Figure 16: Magnified images of the struts of the acetabular implants with a diamond infill. (a) The FG design, with a porosity varying from 90% to 98% porosity seen from top to bottom. (b) The MIN design, with a porosity of 90%. (c) The MIN design with a porosity of 98%.

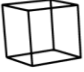## Table 3 Porostity of the non-auxetic meta-biomaterials.
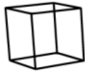
<div align="center">Porosity [%]</div>

<div align="center">As manufactured</div>

Type	C		TC		TCO		RD-YZ		RD-X		D		BCC	
CAD	mean	std.	mean	std.	mean	std.	mean	std.	mean	std.	mean	std.	mean	std.
80	80.00	0.10	80.39	0.18	80.39	0.11	81.50	0.21	80.79	0.18	83.25	0.10	83.81	0.27
85	84.63	0.07	84.14	0.05	84.14	0.03	85.34	0.11	84.80	0.08	87.05	0.03	87.17	0.07
90	89.03	0.09	89.14	0.10	89.14	0.03	89.94	0.10	89.38	0.11	91.21	0.03	90.82	0.07
95	94.04	0.07	93.86	0.01	93.86	0.08	94.16	0.04	93.85	0.06	94.88	0.08	94.81	0.03
98	97.25	0.05	96.60	0.05	96.60	0.08	96.68	0.13	96.68	0.13	97.59	0.08	97.36	0.03

Table 4 Mechanical Properties of the non-auxetic meta-biomaterials.

| Type	Porosity [%]	E [MPa]		σ_{max} [MPa]		σ_{pl} [MPa]		ν	
	CAD	mean	std.	mean	std.	mean	std.	mean	std.
C	80	27.50	1.69	38.85	0.75			0.08	0.03
	85	30.05	2.45	26.63	0.84			0.08	0.04
	90	12.97	1.61	18.53	3.47			0.07	0.02
	95	19.58	1.22	7.32	0.22			0.06	0.01
	98	2.81	1.00	1.37	0.14				
TC	80	22.07	2.70	46.07	2.91			0.07	0.03
	85	11.75	1.01	25.94	0.25			-0.17	0.08
	90	11.64	0.45	15.30	0.48			-0.08	0.17
	95	6.56	0.16	5.74	0.73			-0.04	0.08
	98	1.39	0.16	1.17	0.05			0.41	0.11
TCO	80	16.47	0.51	34.08	0.57			0.31	0.04
	85	10.96	1.16	25.53	0.26			0.46	0.04
	90	5.53	0.28	13.25	0.10	10.36	0.45	0.52	0.01
	95	1.78	0.03	3.86	0.05	3.32	0.13	0.45	0.02
	98	0.69	0.04	1.78	0.03	1.42	0.06	0.70	0.07
RD-YZ	80	10.70	1.26	23.48	4.67			0.67	0.06
	85	7.13	1.15	13.92	3.04			1.16	0.27
	90	2.28	0.35	5.56	1.29	5.56	1.79	1.22	0.06
	95	0.95	0.05	2.77	0.02	2.72	0.05	1.56	0.12
	98	0.09	0.02	0.30	0.05	0.27	0.04	0.94	0.19
RD-X	80	8.71	0.25	24.94	0.84			0.46	0.03
	85	5.32	0.08	15.18	0.26			0.46	0.04
	90	4.38	0.81	6.93	0.15	7.26	0.16	0.49	0.03
	95	0.67	0.06	1.97	0.10	2.19	0.07	0.63	0.00
	98	0.08	0.02	0.32	0.04	0.38	0.05	0.76	0.00
D	80	9.12	0.17	22.58	0.63			0.49	0.03
	85	6.24	0.15	14.89	0.25			0.54	0.01
	90	3.00	0.16	7.49	0.07	5.22	0.30	0.59	0.02
	95	0.86	0.05	2.70	0.05	2.75	0.04	0.65	0.04
	98	0.17	0.01	0.86	0.17	0.83	0.11	0.80	0.06
BCC	80	3.90	0.23	13.79	0.58			0.49	0.03
	85	2.57	0.16	9.00	0.10			0.70	0.03
	90	1.19	0.06	4.65	0.10	4.63	0.11	0.70	0.03
	95	0.31	0.01	1.53	0.02	1.55	0.03	0.75	0.01
	98	0.07	0.02	0.42	0.08	0.43	0.07	0.76	0.05
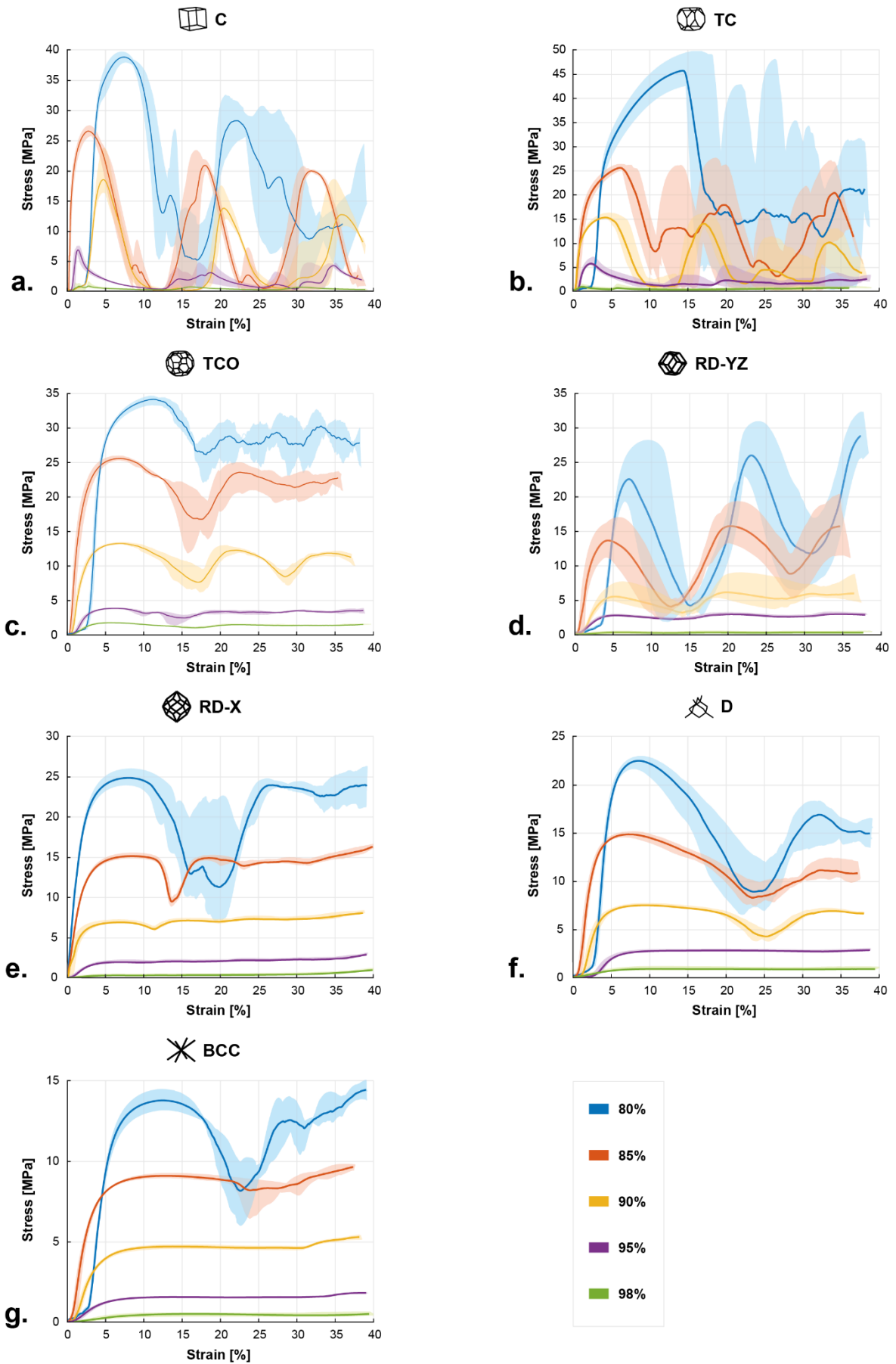
Figure 17: The stress-strain graphs of the non-auxetic meta-biomaterials. The graphs present the mean value and the dispersion the data values.

3.1.2.1 Elastic Gradient (E)

The results for the elastic gradient are presented in Figure 18 and Table 4. There were no outliers in the data of the elastic gradient, as assessed by inspection of a boxplot. The data were normally distributed, as assessed by Shapiro-Wilk's test ($p > .05$). The assumption of homogeneity of variances was violated, as assessed by Levene's test for equality of variances, $p < .01$. However, since the sample sizes are equal and the ratio of the largest group variance to the smallest group variance is less than 3, Jaccard *et al.* 1998 argued that the two-way ANOVA could be performed anyway.[74] Therefore, this statistical test design was continued.

There was a statistically significant interaction between design and porosity for the elastic gradient, $F(24, 103) = 69.162$, $p < .001$, partial $\eta^2 = .942$. Therefore, an analysis of simple main effects for porosity and topological design was performed with a Bonferroni correction.

There was a statistically significant difference in mean elastic gradient scores between the topological designs, $F(6,103) = 858.172$, $p < .001$, partial $\eta^2 = .980$. The differences between the topological designs were most apparent at 80% porosity, $F(6,103) = 366.525$, $p < .001$, partial $\eta^2 = .955$, and least apparent at 98%, $F(6,103) = 5.565$, $p < .001$, partial $\eta^2 = .245$. Pairwise comparison revealed the elastic gradient value of some topological designs do not significantly differ at certain porosities, which can be seen in Figure 18.
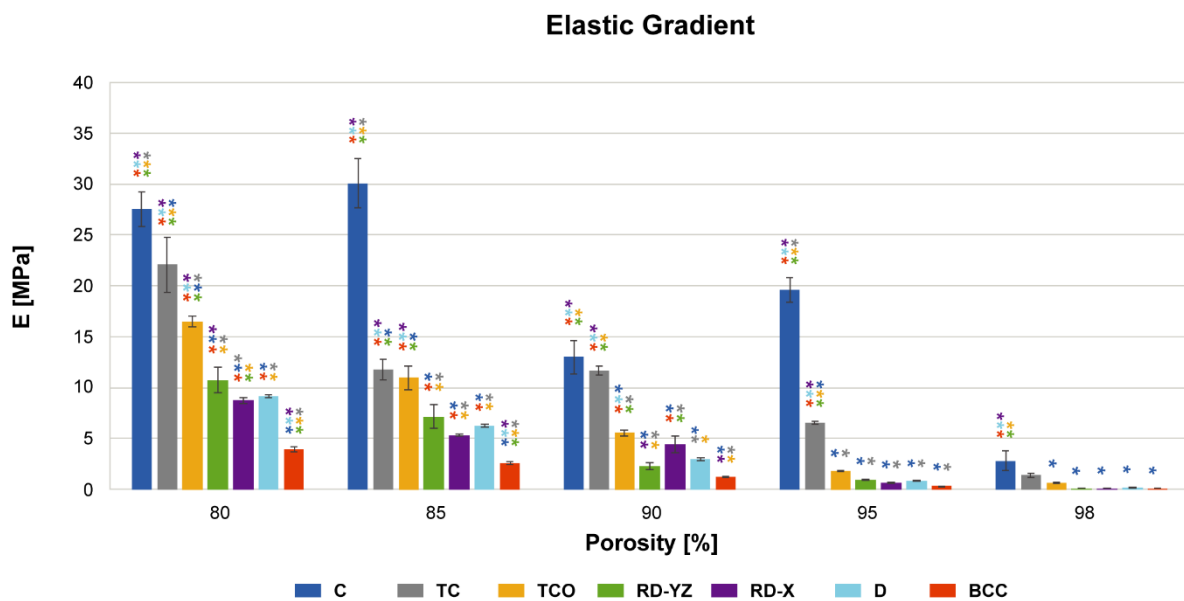

Figure 18: The results on the elastic gradient of the non-auxetic meta-biomaterials. Data is expressed as mean and error bars indicate the standard deviation. Significant differences (p <.05) are indicated by * in the color indicated in the legend.

Next, the effect of porosity on the elastic gradient was determined. There was a statistically significant difference in mean elastic gradient scores between the different porosities for the different topological designs, $F(4,103) = 988.396$, $p < .001$, partial $\eta^2 = .975$. This effect was most apparent for the C, $F(4,103) = 601.568$, $p < .001$, partial $\eta^2 = .959$, and the least apparent for the BCC, $F(4,103) = 13.665$, $p < .001$, partial $\eta^2 = .347$.

3.1.3.2 First Maximum Compressive Strength (σ_{max})

Figure 19 presents an overview of the σ_{max} of all topological designs for all porosities. The results showed no outliers and residuals were normally distributed ($p > .05$). The assumption of homogeneity of variances was violated ($p < .01$). Like the data of the E, the data of the σ_{max} violated the assumption of homogeneity of variances ($p < .001$). Nevertheless, the two-way ANOVA was performed.

There was a statistically significant interaction between topological design and porosity for σ_{max}, $F(24, 103) = 45.822$, $p < .001$, partial $\eta^2 = .914$. Therefore, an analysis of simple main effects for porosity and topological design was performed with a Bonferroni correction.

There was a statistically significant difference in mean σ_{max} scores between the topological designs $F(6,103) = 306.530$, $p < .001$, partial $\eta^2 = .947$. This effect was significant for all porosities ($p < .001$), except for the 98% porosity ($p = .636$). For 80% porosity the difference was most apparent, $F(6,103) = 292.977$, $p < 0.001$, partial $\eta^2 = .945$. Pairwise comparison revealed the σ_{max} value of some topological designs do not significantly differ at certain porosities, which can be seen in Figure 19.
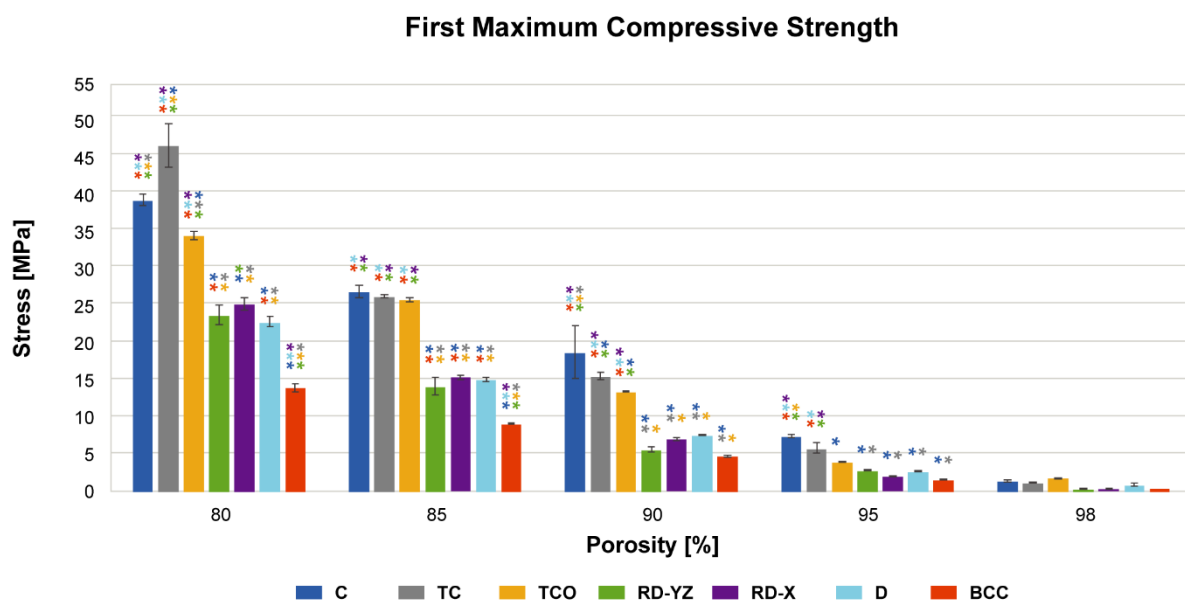

Figure 19: The results on the first maximum compressive strength of the non-auxetic meta-biomaterials. Data is expressed as mean and error bars indicate the standard deviation. Significant differences (p <.05) are indicated by * in the color indicated in the legend.

30

Next, the effect of porosity on the mean σ_{max} scores was determined. There was a statistically significant difference in mean σ_{max} scores between for different porosities, $F_{(4,103)} = 2198.954$, p < .001, partial η^2 = .988. This effect was most apparent for the TC, $F_{(4,103)} = 1288.251$, p < .001, partial η^2 = .964 and the least apparent for the BCC, $F_{(4,103)} = 73.426$, p < .001, partial η^2 = .740.

3.1.3.3 Plateau Stress

The mean plateau stress of the TCO, D, BCC, RD-YZ and RD-X has been presented in Figure 20. There were no outliers, as assessed by inspection of a boxplot. The data were normally distributed, as assessed by Shapiro-Wilk's test (p > .05). The assumption of homogeneity of variances was again violated (p < .001), also in this case the two-way ANOVA was nevertheless performed.

There was a statistically significant interaction between design and porosity for the plateau stress, $F_{(8, 44)} = 20,937$, p < .001, partial η^2 = .792. Therefore, an analysis of simple main effects for porosity and topological design was performed with a Bonferroni correction.

There was a statistically significant effect of topological design on the mean plateau stress, $F_{(4, 44)} = 51,856$, p < .001, partial η^2 = .825. This effect was most apparent at 90%, $F_{(4, 44)} = 87.941$, p < .001, partial η^2 = .825, and the least apparent at 98%, $F_{(4,44)} = 3.019$, p < .05, partial η^2 = .215. Pairwise comparison revealed the plateau stress value of some topological designs do not significantly differ at certain porosities, which can be seen in Figure 20.

Next, the effect of porosity on the mean plateau stress was determined. There was a statistically significant effect of porosity on the mean plateau stress, $F_{(2,44)} = 741.696$, p < .001, partial η^2 =
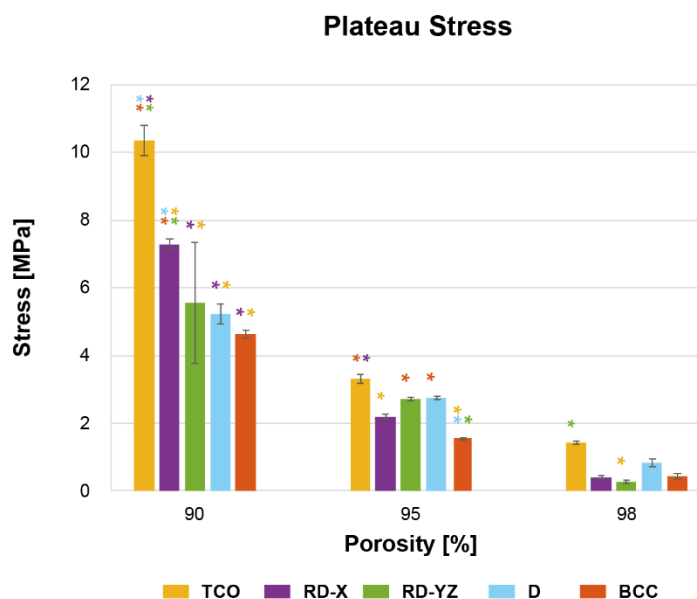

Figure 20: The results on the plateau stress of the non-auxetic meta-biomaterials. Data is expressed as mean and error bars indicate the standard deviation. Significant differences (p <.05) are indicated by * in the color indicated in the legend.

.971. This effect was most apparent for the TCO, $F_{(2,44)} = 334.989$, $p < .001$, partial $\eta^2 = .938$, and the least apparent for the BCC, $F_{(2,44)} = 77.499$, $p < .001$, partial $\eta^2 = .779$.

3.1.3.4 Poisson's Ratio (v)

The mean Poisson's ratio of all lattices has been presented in Figure 21. There were no outliers, as assessed by inspection of a boxplot. The data were normally distributed, as assessed by Shapiro-Wilk's test ($p > .05$). The assumption of homogeneity of variances was again violated ($p < .01$). The two-way ANOVA was nevertheless performed.

There was a statistically significant interaction between porosity and topological design for the Poisson's ratio, $F_{(23, 91)} = 14.103$, $p < .0001$, partial $\eta^2 = .781$. Therefore, an analysis of simple main effects for porosity and topological design was performed with a Bonferroni correction.

There was a statistically significant effect of topological design on the mean Poisson's ratio, $F_{(6, 91)} = 339.258$, $p < .001$, partial $\eta^2 = .957$. This effect was most apparent at 95%, $F_{(6, 91)} = 148.390$, $p < .001$, partial $\eta^2 = .907$, and the least apparent at 98%, $F_{(5,91)} = 18.482$, $p < .001$, partial $\eta^2 = .504$. Pairwise comparison revealed the Poisson's ratio of some topological designs do not significantly differ at certain porosities, which can be seen in Figure 21.

Next, the effect of porosity on the Poisson's ratio was determined. There was a statistically significant effect of porosity on the mean Poisson's ratio for all unit cells ($p < .001$) except for the C ($p = .966$) This effect was most apparent for the RD, $F_{(4,91)} = 64.883$, $p < .000$, partial $\eta^2 = .740$.
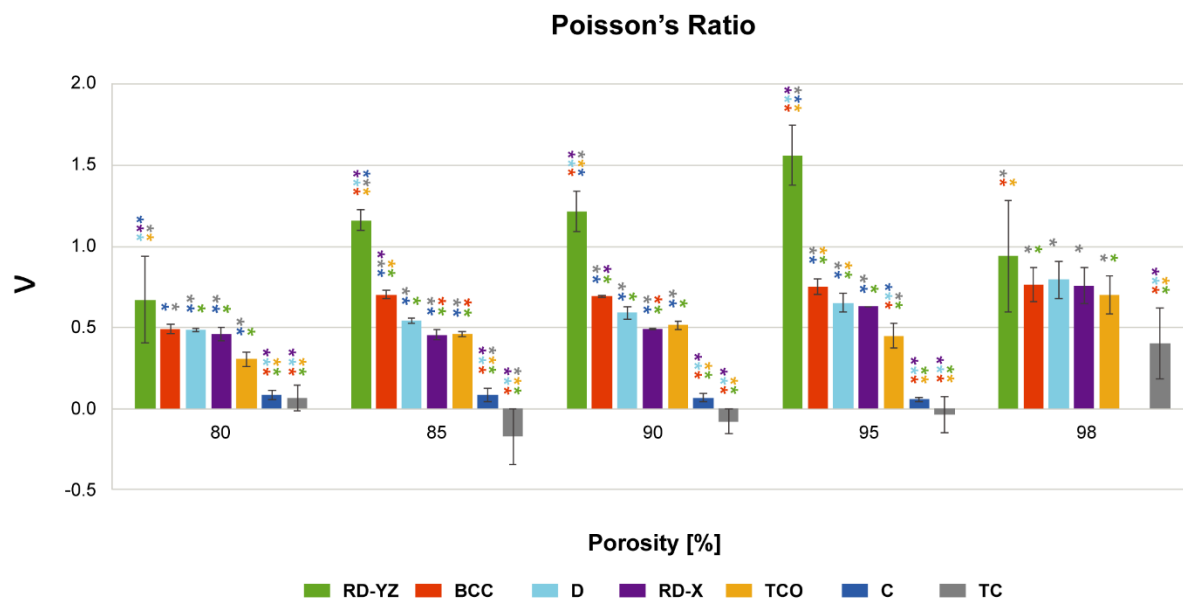

Figure 21: The results on the Poisson's ratio of the non-auxetic meta-biomaterials. Data is expressed as mean and error bars indicate the standard deviation. Significant differences (p <.05) are indicated by * in the color indicated in the legend.

3.2 Acetabular Implants

3.2.1 Morphological Properties

The morphological properties of the acetabular implants have been presented in Table A2 and A3 (Appendix). In general, the porosity as-manufactured (measured by the dry weighing technique and µCT) is lower than the designed porosity. In any case this difference did not exceed 3%.

3.2.2 Mechanical Properties

All acetabular cups were tightly fixed in the moulds after the compression tests. Figure 22 shows the load-deformation curves of the nine different designs. The curves are very similar for the acetabular cups within the same sample group (unit cell and porosity). The three topological designs (BCC, D, RD) showed consistent results, which was reflected in the fact that the highest push-in forces were measured for the acetabular cups with the lowest porosity (MIN), while the lowest push-in forces were observed for the acetabular cups with the highest porosity (MAX). A bulging effect of the unit cells not in contact with the mould (the bottom of the cup) could be observed in the MAX designs (Figure 23). The acetabular cups with a functionally graded (FG) porosity showed push-in forces in between the other two porosities. In all three design types (MIN, MAX, FG) the measured push-in force followed the order RD, D, BCC.
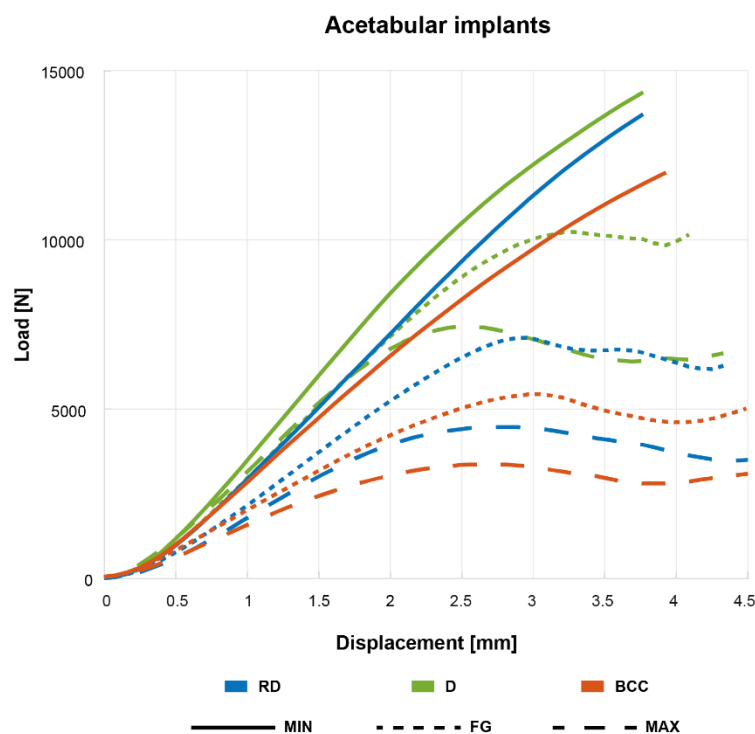

Figure 22: Load-displacement graph of the acetabular implants with the three different unit cell types and three different porosities.
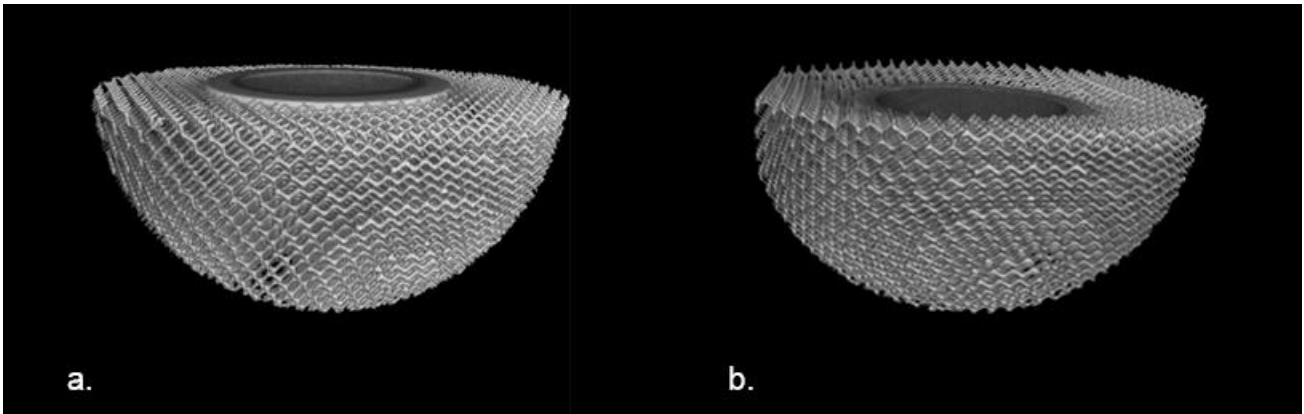
Figure 23: A 3D representation of the MAX design (98%) of the diamond unit cell, (a) before compression, (b) after compression. After compression a bulging effect can be observed at the bottom of the cup.

3.2.3 Deformation

The samples of each of the three different designs (MIN, MAX, FG) showed quite consistent results regarding the deformation of the porous layer inside the mould. This was the case for all three unit cell types. This can be observed in the µCT scans presented in Figure A2 (Appendix). 3D representation of all designs can be observed in Figure A3. Another way to observe the deformation is by evaluating the degree of anisotropy (DA) within the porous layer. Table 5 presents the difference in DA before and after compression. The effect of the compression of the implant on the mould can most optimally be observed after cutting the moulds in half (Figure A3).

Type		Degree of Anisotropy				Difference [%]
		BEFORE	std.	AFTER	std.	
BCC	MIN	0.173	0.009	0.152	0.007	11.77
	MAX	0.184	0.054	0.137	0.007	19.66
	FG	0.161	0.011	0.100	0.007	19.24
D	MIN	0.153	0.009	0.159	0.003	-3.85
	MAX	0.138	0.054	0.064	0.028	52.30
	FG	0.118	0.011	0.080	0.023	32.93
RD	MIN	0.389	0.031	0.362	0.038	5.86
	MAX	0.537	0.036	0.506	0.008	4.59
	FG	0.493	0.048	0.383	0.038	22.14

Table 5 Degree of anisotropy before and after compression for the different acetabular implant designs

<div align="right">

4

</div>

<div align="right">

Discussion

</div>

The aim of this study was to design a deformable porous acetabular implant which plastically deforms into massive acetabular defects. Six unit cell designs have been evaluated to determine their potential application in such an implant. In order to determine their mechanical properties, static compression tests have been performed. Additionally, the Digital Image Correlation (DIC) technique has been used to evaluate both the Poisson's ratio and deformation mechanism of the unit cells. Based on their space-filling properties, three unit cell types have been implemented in the design of the acetabular implant. This design consisted of a solid inner layer connected to a porous outer layer which had a unit cell based infill. Three designs have been manufactured, including two uniform porous implants and one functionally graded porous implant. These designs have been tested in an experimental set-up that simulates an acetabulum with large bone defects. The results of both subprojects will be thoroughly discussed in the following paragraphs. Additionally, the challenges and limitations that had to be faced during this project will be described. In the end the potential application of the presented concepts and future required work will be presented.

4.1 Non-auxetic Meta-biomaterials

4.1.1 Morphological Characterization

The porosity of the non-auxetic meta-biomaterials was determined after manufacturing (Table 3). The results show that the designed porosity (CAD) and the manufactured porosity do not exactly overlap. In general the porosity as-manufactured is lower than the CAD porosity, except at 80% porosity. An explanation for this difference might be metal powder that partially gets fused to struts' surface. This powder adds weight to the final sample, which affects the measured porosity. The difference between designed and manufactured porosity increased with increasing porosity, which is the case for all unit cells. This can be explained by the fact that the size of the imperfections (i.e. powder particle adhesion on the struts) caused by the AM process is presumably more or less stable for different strut thickness.[75] This means that the effect of imperfections is more predominant for thinner struts and thus higher porosities. Additionally, the difference between the designed

porosity and the porosity as-manufactured was not the same for all unit cell types. This difference was most apparent for the BCC (mean difference 1.8%) and the least for the C (means difference 0.66%). The mechanical properties of the different unit cell types are compared based on the designed porosity. Since the porosity as-manufactured is not exact the same as the designed porosity, there are small difference in porosity between the compared unit cells types. Nevertheless, these differences are neglectable small.

4.1.2 Mechanical Properties

In this study the terms "elastic modulus", "first maximum compressive strength", "plateau stress" and "Poisson's ratio" has been used for the mechanical properties of the non-auxetic meta-biomaterials. However, it is important to understand that these terms describe different concepts when they concern meta-biomaterials. In the case of traditional materials these terms evaluate the intrinsic properties of the material, while when referring to meta-biomaterials they describe the apparent macroscopic properties of its structures instead of its material.[26]

In this study commercially pure titanium (CP-Ti) has been used instead of more commonly studied titanium alloy (Ti-6Al-4V). CP-Ti has been reported to show higher ductility as well as a constant deformation under compression without reaching a first local maximum.[31, 76] Besides, the fatigue strength of CP-Ti is also found to be higher compared to its alloyed counterpart.[31, 77] No difference between the two material types have been found for bone response, bacterial adhesion and corrosion resistance.[78] A biological advantage of CP-Ti is the absence of hazardous alloy component including V and Al.[31] Several studies have used CP-Ti in combination with lattice structures [31, 76-82], however a systematic evaluation of the topology-property relationship of different unit cell types, as performed in this study, has not been done before. Therefore the results of this study could only partly be verified with results from the literature. Nevertheless, the results will also be verified with experiments that used alloyed titanium.

The non-auxetic meta-biomaterials were tested in axial compression, resulting in the stress-strain curves presented in Figure 17. These curves show different patterns, which can be explained based on the unit cell's topological design and the resulting deformation mechanisms (Figure A1, Appendix). The deformation mechanism of lattices is usually a combination of bending and stretching.[47, 83] Which deformation mechanism is dominating depends on the main strut orientation. [47, 83] Unit cells for which this orientation is mainly aligned along the loading direction present stretch-dominated deformation behaviour. These lattices show very brittle behaviour, leading to high load bearing capacities. Their deformation pattern is dominated by a layer-by-layer collapse, which results in stress drops after which stress is built up again.[84] This behaviour can be seen for the C, TC and the lowest porosities (80% and 85%) of the RD-YZ and TCO. Lattices with a more inclined

main strut orientation show a bending-dominated deformation pattern. These geometries are characterized by more ductile behaviour, leading to a lower load bearing capacity.[47, 83] This deformation pattern is presented by the BCC, D, RD-X and the lattices with higher porosities (90%, 95% and 98%) of the RD-YZ and TCO. Their stress-strain curve presents a gradual increase in stress followed by a plateau. In most cases a shear band at an angle of 45° is observed in the deformation pattern. The deformation pattern of the lattice structures is fairly similar over the complete range of porosities for most unit cell designs, which means that the deformation mechanism is independent of the porosity. One remarkable exception to this is the TCO. The 80%, 85% and 90% porosity lattices show a clear compression-deformation pattern, while the 95% an 98% porosity lattices show completely different deformation patterns. The latter present a bending-dominated deformation pattern, which even results in auxetic behaviour. The TCO unit cell was not expected to show auxetic behaviour, since this cell was reported show non-auxetic behaviour in studies based on titanium alloy. This remarkable behaviour might be explained by the higher ductility of CP-Ti compared to its alloyed counterpart. All other non-auxetic meta-biomaterials have showed deformation patterns which are in line with the literature.[30]

The elastic gradient and the first maximum compressive strength were extracted from the obtained stress-strain curves. Both properties are found to increase with decreasing porosity for all topological designs, which was expected according to the model of Gibson and Ashby.[46] For the gradient there was one exception to this relationship, the C unit cell showed some irregularities in this trend. A possible explanation for this is the fact that the lattices of the C were not tested on the same compression machine. The C 80% and the C 90% were tested on the 250 kN test machine, while the other samples were tested on the 20 kN machine. The results from both machines were corrected for machine compliance. After this correction the results of the 80% and 90% deviated a bit from the trend seen for the other samples of this design. In general it was intended to test each specimen on the most appropriate compression machine. This means that the expected maximal compression force of the sample and the maximal test force of the machine should not deviate too much. Since the expected maximal compression force of the samples increases with decreasing porosity, it was the intended to test the samples with the lowest porosity on the 250 kN compression machine and the samples with the highest porosity on the 20 kN or 10 kN compression machines. The C is the only topological design for which this was mixed due to availability of the machines. This is expected to be the reason for the irregularity in the relationship between porosity and elastic gradient.

Two groups of unit cells could be distinguished when considering the elastic gradient for all designs: a group with high stiffness, including the C, TC and TCO unit cells, and a group with lower stiffness, including the RD-X, RD-YZ, D and BCC. Values ranging from 0.07 to 30.05 MPa have been found

(Table 4). In general the C showed the highest stiffness, while the BCC showed the lowest stiffness. The results found in this study followed the same trend as found in literature.[30] Within the group with lower stiffness there is not much difference between the different unit cell designs, especially for high porosities (> 95%). In the literature it is described that the RD unit cell presents a different elastic gradient in the two main directions, with a higher stiffness in the RD-YZ direction.[30, 54] The results found in this study confirm this with a significantly higher value for RD-YZ compared to RD-X at 80% and 90% porosity. The CP-Ti lattices showed lower elastic gradient values compared to their alloyed counterparts studied in the literature.[30]

The first maximum compressive strength showed also increasing values with decreasing porosity. This effect was even more pronounced compared to the elastic gradient. Values from 0.3 to 46.07 MPa have been found (Table 4). The same two groups, as found for the elastic gradient, could be distinguished. The RD-YZ, RD-X, D and BCC consistently showed the lowest strength. The RD-YZ and RD-X were not significantly different from each other, which is supported by literature.[30, 54] The C, TC, TCO make up the group with the highest strength. The results found followed the same order as found in literature.[30] The strength of the CP-Ti lattices is lower compared to Ti-6Al-4V lattices studied in the literature, which was expected.[30]

The plateau stress has only been examined for the lattices that presented a plateau after reaching the first maximum compressive strength (BCC, RD-YZ, RD-X, TCO and D). Values from 0.27 to 10.36 MPa have been found (Table 4). It has been argued in the literature that the plateau stress is similar to the yield stress when it concerns porous structures.[50, 85, 86] The ratio between the first maximum compressive strength and the plateau stress is very constant and close to one for the BCC and RD-YZ. For the other unit cell types, this ratio was stable but it was either slightly higher (RD-X) or lower (TCO and D) than one. These results indicate that the BCC, RD-YZ, RD-X, TCO and D show stable strength after reaching the first maximum compressive strength.

Regarding the Poisson's ratio, an increasing porosity resulted in an increasing value for the Poisson's ratio in all unit cell designs. Remarkable results were found for the RD-YZ and TC. The lattices of the TC present a negative Poisson's ratio for the 85%, 90% and 95% lattice structure. This was not expected since this unit cell has been reported as non-auxetic (positive Poisson's ratio) in literature.[30, 53] The RD-YZ structures, on the other hand, showed a Poisson's ratio above 1 for the 85%, 90% and 95% porous structures. The samples with 98% porosity of the RD-YZ disrupted the increasing trend of the Poisson's ratio. A possible explanation for this will be explained in the limitation section of this discussion. In the other direction (RD-X) the Poisson's ratio ranges from 0.455 to 0.759 for the complete range of tested porosities. In the literature, conflicting results are found for this unit cell design. Babaee *et al.* (2012) reported values of ± 0.5 for the RD-X and ±

1.0 for the RD-YZ, while another study with computational results pointed at values ranging from 0.42 to 0.56 for RD-YZ and values from 0.36 to 0.40 for RD-X.[30, 54, 87] The Poisson's ratio values found for the RD (both directions) unit cell are not exactly overlapping with the results found in the literature (based on Ti-6Al-4V).[30, 54, 87] However, the significant difference between the two directions is the same as found in the literature.[30, 54, 87]. For all other topological designs the Poisson's ratio ranges from 0.05 to 0.795 (Table 4). When arranged from high to low value, the resulting order is BCC, D, TCO, and C. This order can be explained based on the deformation behaviour. Unit cells with a bending-dominated behaviour presented a higher Poisson's ratio compared to stretch-dominated unit cells. The same order is found in studies based on analytical and computational methods.[30] This study is the first to experimentally study the Poisson's ratio. Therefore it is hard to verify the results with the literature. The Poisson's ratio for traditional materials ranges between -1.0 and +0.5 for isotropic materials.[88] The results of the non-auxetic meta-biomaterials found in this study presented values above this range, which shows that these results are the apparent macroscopic properties of the structures and not of the material itself.[26] A preliminary computational study from the KU Leuven also presented values for the Poisson's ratio out side the traditional isotropic range.

The D, BCC and RD unit cells were chosen to be implemented in the acetabular implants based on their space-filling capacity. These unit cell types showed the best combination between high strength and low stiffness. Additionally, these topological designs presented high ductility which is reflected in the high values for the Poisson's ratio. These unit cells also reached a plateau after reaching their maximal stress. This indicates plastic deformation without the failure of struts.

4.2 Acetabular Implants

4.2.1 Morphological Characterization

Comparable to the non-auxetic meta-biomaterials the as-manufactured porosity is generally lower than the CAD porosity for the acetabular implants. As mentioned earlier, the metal powder sintered to the struts during printing probably caused this. This effect might also be the explanation for the fact that the strut thickness as-manufactured is thicker than the CAD strut thickness, as assessed by the μCT scans.

The porosity of the MAX design and the most outer layer of the FG design are printed in the minimal printable strut thickness, which is 200 μm.[57] For both the D and BCC this means that the porosity is 98%, while for the RD this is 96% (Table A2 and A3, Appendix). This difference is caused by the fact that the RD consists of more struts, which means the same strut thickness results in a lower porosity.

The RD designs also differed from the D and BCC cups regarding the degree of anisotropy. The geometries of both the D and BCC are isotropic, which is also reflected in low values for the degree of anisotropy determined at the µCT pre-scan. The RD unit cell has a transversally isotropic geometry, which is reflected in different properties in one direction to the other two.[54, 55, 89] This behaviour is also mirrored in the degree of anisotropy (Table 5) which is significantly higher compared to the D and BCC.

4.2.2 Mechanical Properties

When comparing the load-deformation curves of the three unit cell types, it can be observed that for all three porosities (MIN, MAX, FG) the RD showed the highest push-in forces, while the BCC presented the lowest push-in forces. The D showed results in between the other two topological designs. The results for these three unit cells showed the same order as found in the non-auxetic meta-biomaterials. The BCC consistently showed to be the least stiff and the least strong unit cell of the three in both experiments. Although the mechanical properties of the D and RD were very similar in the non-auxetic meta-biomaterials, both unit cells showed a more pronounced difference in push-in force for the acetabular implants. This difference in push-in force is mainly observed in the FG and MAX designs. This can be explained by the fact that the porosity of the RD was designed to be slightly lower (due to AM constraints) compared to the D in both designs. This difference in porosity was not designed for the MIN design, which means that the difference in push-in force is less pronounced for this design type.

4.2.3 Deformation

The three different designs (FG, MIN and MAX) showed three clearly distinguishable deformations which were similar for all unit cell designs. The MAX designs deformed the most, which was also reflected in the degree of anisotropy (Table 5). µCT scan evaluation showed that the deformation mainly took place in the struts directly connected to the solid inner layer. This means that the struts connecting to the solid inner layer fail, after which the solid inner layer is compressed through the porous outer layer. This results in a bulging effect on the bottom layer of the cups (Figure 23). The porous outer layer does not deform into the defects in the mould. After cutting through the mould, it can be seen that the mould is not affected by the compression.

The MIN designs showed the opposite of the MAX designs by showing almost no deformation. This was also reflected in the smallest percentual difference in DA after compression (Table 5). After cutting the moulds in half after compression, it could be observed that he moulds were deformed by the acetabular cups. This means that the acetabular cups with the minimal porosity (MIN) are too stiff for the moulds.

The FG designs showed some deformation at the implant-mould interface, without collapsing struts at the interface between the solid layer and the porous layer. The unit cells directly in contact with the mould are deformed into the holes (Figure A3, Appendix). This deformation is clearly detectable, but not tremendous. This could also not be expected since the cups were only compressed for approximately five mm. The deformation is the most for the diamond, which is also reflected in the highest percentual difference of DA (Table 5). The unit cells in contact with the solid inner layer are unaffected, which contrasts with the same unit cells in the MAX designs. After cutting the moulds in half it could be observed that the mould is only slightly affected by the compression of the acetabular cup (Figure A4, Appendix). This means that this acetabular cup design possesses the mechanical properties which are like the properties of the mould and thus to healthy trabecular bone.

As beforementioned does the RD unit cell have a transversally isotropic geometry. In the acetabular implant the RD unit cell was oriented in such a way that the main loading direction was in the RD-YZ direction. Due to its transversally isotropic geometry, its deformation inside the mould would theoretically be not the same in each direction. This effect was not observed on the CT scans. However, it is expected that this effect increases as the implant is compressed for more than five mm.

Since this research is of a highly explorative nature, there is no literature available on how to determine the degree of deformation of this kind of porous deformable implants. Therefore, we had to came up with a method to quantify this. The chosen approach was to determine the degree of anisotropy (DA). This method evaluates how highly oriented structures are, using the mean intercept length technique. The DA ranges from 0 to 1, from isotropic to anisotropic structures.[69] The acetabular implants became more isotropic after compression according to this method. This effect was not expected. A possible explanation might be that the compressed struts are more oriented in one direction compared to their non-compressed counterparts.

4.3 Challenges and Limitations

Most of the procedures that have been followed in the first part of this study (non-auxetic meta-biomaterials) are broadly known in the literature. However, the use of DIC is quite new when studying lattice structures. Some studies used this technique to determine the strain distribution in these kind of structures.[48, 90-92] In this study this technique was used to experimentally determine the Poisson's ratio, which only a few studies did before.[48, 72] In some cases the reliability of the DIC technique is questionable. This is mainly the case for the porous structures with the thinnest struts (98%). For these struts there is only a limited number of pixels on the strut to track the deformation. Furthermore, the elastic region is of these samples is very short, which means that there is only

limited time and thus limited images to determine the Poisson's ratio. This also does not improve the reliability of the Poisson's ratio. Both effects could be an explanation for the remarkable results found for the Poisson's ratio of the RD-YZ 98%. In case of the C 98% samples it was not possible at all to determine the Poisson's ratio, even after manual determination using photoshop. In this case the elastic deformation before failure was to small to be detected. [93] For the samples with thicker struts the DIC technique is a quite reliable technique to determine the Poisson's ratio, which could be concluded based on the small inter-specimen differences. However, recently Acciaioli *et al.* (2018) argued that this technique slightly overestimates the values with 4%.[93] Also the VIC 3D software presents an higher projection error in these cases. This should be considered when interpreting these results.

Another limitation in the procedure of the first experiment is the fact that the non-auxetic meta-biomaterials are only compressed in the build direction. Although most of the unit cell types that are considered are isotropic, based on their geometry, the print process is found to introduce a certain level of anisotropy to the structure.[94, 95] Especially struts that are build horizontally with respect to the build plate are prone to show AM imperfections.[96] These struts are found to have more internal porosity, which results in diminished mechanical properties.[96, 97] In order to get the complete overview of mechanical properties of the non-auxetic meta-biomaterials, it is important to evaluate them in all directions.

The procedures followed in the second part of this study are less commonly used. Due to the explorative nature of this part of the study there is no literature to fall back on. To our knowledge the present study is the first attempt to additively manufacture a deformable functionally graded acetabular implant. Earlier this idea was presented by Wang *et al.* (2006), but it was never actually executed.[98] In order to test the deformability of the implant a mould made of bone mimicking foam has been used.[67] This material was chosen over cadaveric bone due to the possible uniformity, low inter-specimen variability, reproducibility and to avoid ethical issues. This artificial bone material has a Young's modulus of 0.137 GPa.[67] Healthy trabecular bone presents stiffness values in the range of 0.02 to 2 GPa.[99] However, the aim of this project is to design an acetabular implant for patients with large acetabular bone deficiencies. The mechanical properties of their bone quality will probably not be as good as healthy trabecular bone. In some cases their bone might be of poor (osteoporotic) quality. Therefore the used material of the mould might not exactly represent this situation. Patel *et al.* (2008) argued that cellular rigid polyurethane foam with a lower density (PCF 10, 0.16 g/cm^3) might better resemble osteoporotic human trabecular bone.[100] This type of foam presents a stiffness of 0.05 GPa.[67]

Another limitation found in the second part of this study are the high maximal push-in forces (ranging from 3.33 kN to 14.8 kN) needed to compress the acetabular implants for only five mm into the moulds. These forces were applied under a constant deformation rate of 0.5 mm/min. For a surgeon it is impossible to apply this kind of force at such a low deformation rate. In the conventional surgical procedure the implant is inserted using impact force. The mean impact force given during this procedure is 16.75 kN with maximal peak forces of 27.49 kN. The mean impact force is applied five times on average.[101] It is our expectation that this way of implementing is not applicable on the newly designed acetabular implants. Impacting the implant will lead to unpredictable deformation. Besides it might also break struts, which is undesirable. Loose struts can become metal debris which could induce inflammatory reactions at the bone-implant interface.[102] Therefore a new surgical procedure has to be developed for this kind of deformable implants. This new procedure should be able to apply a push-in force that is high enough to deform the implant. It is obvious that this force should not be too high in order not to break through the pelvis. A possible option might be the application of several screws at the edges of the implant which are simultaneously tightened. When the surgeon has the opinion that enough initial stability is attained, the screws can be removed to prevent stress-shielding. The screw holes can be filled again with porous titanium.

4.4 Potential Applications

The first part of this study (non-auxetic meta-biomaterials) adds knowledge to the growing library about the topology-property relationship of lattice structures. It does so by experimentally determining the mechanical properties of these materials, including the Poisson's ratio. Furthermore, the novelty of this study lies in the use of CP-Ti as the material type. The results provide information to facilitate the selection of the most appropriate biomaterial for an envisioned implant application. Additionally, these results can be used to verify computational and numerical studies on this kind of structures.

The second part of this study concerns a first explorative study on the deformability of a porous acetabular implants. It also provides information about the effect of functionally grading porosity in this kind of implants. The three different acetabular implant designs showed three different deformation behaviours as well as three different load-displacement curves. The MIN and MAX designs showed, respectively, almost no deformation and undesired deformation. The results found for these two designs present a clear range of properties in which this type of deformable implant can perform. The FG designs showed a more promising deformation, with the most favourable results found for those built of diamond unit cells.

This functionally graded porous acetabular implant could potentially be applied in acetabula with large bone deficiencies. The designs in this study are evaluated on defects in which the medial wall

of the acetabulum is still intact. This corresponds to defects such as Paprosky Type 1, Type 2a and Type 2b. This type of implants could potentially also be applied in situation in which the medial wall of the acetabulum is not intact. In this case the remaining bone will prevent the implant from going through the pelvis. The implant will plastically deform into the bone defects, which will result in a large bone-implant interface which results in adequate biological fixation. This will contribute to a more physiological load distribution compared to the currently used acetabular implants with flanges. The porosity of the outer layer will furthermore result in comparable stiffness between the bone and the implant. This diminishes the effect of stress-shielding, and therefore prevent bone resorption. This implant could be applied in combination with a dual mobility cup design which will then be cemented into the porous layer. This system is also used in custom-made triflange implant.[103] On the long term a deformable acetabular implant might also become the standard in primary hip replacing surgery.

Besides applying the porous structures in an acetabular implant, there are many other biomedical applications. One could think of non-load bearing applications like a cranio-maxillofacial implant.

4.5 Future Work

In this study only static compression was considered. The designed acetabular implants should be able to stay in the body for at least ten years after implantation. Therefore it is very important to asses their fatigue behaviour as well. The implants will mostly be loaded in compression, so compression-compression fatigue tests are most interesting.[26, 104] There are some data on the fatigue behaviour of CP-Ti porous structures[77, 78], but a systematic study is missing. This might be a subject for future work.

At this moment quite a large force is needed to deform the porous layer for only five mm. In order to increase the deformation of the acetabular implant, several designs decisions could be studied in the future. Firstly, the infill of the porous outer layer. A larger unit cell size while keeping the strut size equal to the current strut size increases the porosity and might therefore increase the deformability. When studying the effect of unit cell size (unpublished work by Groenewoud *et al.* 2017), it can be seen that the relationship between unit cell size and stiffness is exponential. This means that increasing the unit cell size from 3x3x3 mm to for example 5x5x5 mm will result in a in an approximately 200 times lower stiffness. This change in design will diminish the number of layers in the outer layer, which means that the porosity transitions have to occur within the unit cells. In this study this was not possible, due to software constraints. There is an option to design continuously changing porosity within the unit cells by using a sigmoid function. Researchers at the KU in Leuven are currently working on this.

The infill of the porous outer layer could also be designed differently by using other unit cell types. In this study the most deformable strut-based unit cells were used. An alternative might be structures based on triply periodic minimal surfaces (TPMS), whose surface curvature is believed to mimic that of trabecular bone.[105] Structures based on TPMS show a promising combination of high strength and low stiffness.[25] Therefore it might be interested to test the deformability of this kind of unit cells.

Another design choice that is interesting to study in the future is the choice of material type. A possible option for this might be pure iron.[106] Recently Li *et al.* (2018) found relatively low values for stiffness for porous iron structures with a 1x1x1 mm unit cell size.[106] When extrapolating this to 5x5x5 mm unit cells the stiffness values might be interesting to implement into the acetabular cup design. Decreased stiffness will decrease the force needed to deform the material. Annealing pure iron material decreases the stiffness even more.[107]

Once the ideal deformable acetabular implant is developed, it is essential to determine its biological effect on living bone tissue. Furthermore, it is important to evaluate the effects of time-dependent phenomena such as bone regeneration and ingrowth.[26]

5
Conclusion

The objective of this study was to design and evaluate a new concept for an acetabular revision, which on the long term could also become the standard in primary hip replacing surgery. The aim of this new acetabular implant design is to plastically deform into massive acetabular bone defects. This novel implant has the potential to overcome most of the complications observed after an acetabular revision. This study explored whether a unit cell based porous outer layer made of pure titanium can achieve the required space-filling properties. After studying the topology-property relationship of six potential unit cell designs, three topologies were selected including the diamond, rhombic dodecahedron and body centred cubic. These unit cells showed the lowest stiffness and the highest positive Poisson's ratio over the complete range of concerned porosities (80-98%). Besides, they showed bending-dominated deformation without the failure of struts. The results indicated that these unit cells have the highest capacity to deform as well as space-filling behaviour. Therefore, they were implemented in the design of the deformable acetabular implant. These implants were compressed inside a bone-mimicking mould, of which the appearance and mechanics resembled an acetabulum with large bone deficiencies. µCT images revealed that the novel implant designs showed detectable deformation at the implant-mould interface, without failing struts. The most promising deformation was observed in the implant with a functionally graded porosity based on the diamond unit cell. Although the deformation at the mould-implant interface was promising, the push-in forces needed to compress the implant into the mould were very high (ranging from 3.33 kN to 14.8 kN). Future work is needed to diminish the need for these high push-in forces by making the porous outer layer even more deformable. This novel implant has the potential to increase the biological fixation, preserve the physiological stress distribution and diminish the effect of stress shielding in the acetabular component of a total hip replacement.

6
Abbreviations

THA	Total Hip Arthroplasty
AM	Additive Manufacturing
SLM	Selective Laser Melting
EBM	Electron Beam Melting
CP-Ti	Commercially Pure Titanium
DIC	Digital Image Correlation
FG	Functionally Graded
FOV	Field Of View
D	Diamond
C	Cube
TC	Truncated Cube
TCO	Truncated Cuboctahedron
RD	Rhombic Dodecahedron
BCC	Body Centred Cubic
DMP	Direct Metal Printing
CAD	Computer Aided Designs
STL	Stereolithography
EDM	Electrical Discharge Machining
PCF	Polyurethane Foam
MP	Mega Pixel
µCT	Microtomography
ROI	Region Of Interest
DA	Degree of Anisotropy
N	Newton
kN	Kilo Newton
ν	Poisson's Ratio
ε	Strain
σ	Stress

7
Bibliography

1. K. J. Bozic, S. M. Kurtz, E. Lau, K. Ong, T. P. Vail and D. J. Berry, *The Journal of bone and joint surgery. American volume*, 2009, **91**, 128-133.
2. S. Kurtz, K. Ong, E. Lau, F. Mowat and M. Halpern, *JBJS*, 2007, **89**, 780-785.
3. S. M. Kurtz, E. Lau, K. Ong, K. Zhao, M. Kelly and K. J. Bozic, *Clinical Orthopaedics and Related Research®*, 2009, **467**, 2606-2612.
4. R. H. Choplin, C. N. Henley, E. M. Edds, W. Capello, J. L. Rankin and K. A. Buckwalter, *Radiographics*, 2008, **28**, 771-786.
5. G. K. Deirmengian, B. Zmistowski, J. T. O'neil and W. J. Hozack, *JBJS*, 2011, **93**, 1842-1852.
6. W. G. Paprosky, S. H. Weeden and J. W. Bowling Jr, *Clinical Orthopaedics and Related Research (1976-2007)*, 2001, **393**, 181-193.
7. L. Pulido, S. R. Rachala and M. E. Cabanela, *International Orthopaedics*, 2011, **35**, 289-298.
8. M. Baauw, M. L. van Hooff and M. Spruit, *JBJS reviews*, 2016, **4**.
9. A. Q. Ahmad and R. Schwarzkopf, *Journal of orthopaedics*, 2015, **12**, S238-243.
10. M. A. Wind, Jr., M. L. Swank and J. I. Sorger, *Orthopedics*, 2013, **36**, e260-265.
11. G. E. Holt and D. A. Dennis, *Clinical Orthopaedics and Related Research®*, 2004, **429**, 209-214.
12. R. Huiskes, H. Weinans and B. van Rietbergen, *Clinical Orthopaedics and Related Research*, 1992, 124-134.
13. M. J. Taunton, T. K. Fehring, P. Edwards, T. Bernasek, G. E. Holt and M. J. Christie, *Clin Orthop Relat Res*, 2012, **470**, 428-434.
14. A. B. Joshi, J. Lee and C. Christensen, *The Journal of Arthroplasty*, 2002, **17**, 643-648.
15. D. R. Sumner, *Journal of Biomechanics*, 2015, **48**, 797-800.
16. J. D. Bobyn, E. S. Mortimer, A. H. Glassman, C. A. Engh, J. E. Miller and C. E. Brooks, *Clin Orthop Relat Res*, 1992, 79-96.
17. R. Huiskes, R. Ruimerman, G. H. van Lenthe and J. D. Janssen, *Nature*, 2000, **405**, 704-706.
18. H. M. Frost, *The Angle Orthodontist*, 1994, **64**, 175-188.
19. H. M. Frost, *Charles C. Thomas*, 1964.
20. J. D. Currey, *The mechanical adaptations of bones*, Princeton University Press, 2014.
21. E. Ozcivici, Y. K. Luu, B. Adler, Y.-X. Qin, J. Rubin, S. Judex and C. T. Rubin, *Nature Reviews Rheumatology*, 2010, **6**, 50.
22. Z. G. Nicolaou and A. E. Motter, *Nature materials*, 2012, **11**, 608.
23. A. A. Zadpoor, *Materials Horizons*, 2016, **3**, 371-381.
24. H. M. Kolken and A. Zadpoor, *RSC Advances*, 2017, **7**, 5111-5129.
25. F. S. L. Bobbert, K. Lietaert, A. A. Eftekhari, B. Pouran, S. M. Ahmadi, H. Weinans and A. A. Zadpoor, *Acta Biomaterialia*, 2017, **53**, 572-584.
26. A. A. Zadpoor, *Acta Biomaterialia*, 2019, **85**, 41-59.
27. M. Vaezi, H. Seitz and S. Yang, *The International Journal of Advanced Manufacturing Technology*, 2013, **67**, 1721-1754.

28. F. P. W. Melchels, M. A. N. Domingos, T. J. Klein, J. Malda, P. J. Bartolo and D. W. Hutmacher, *Progress in Polymer Science*, 2012, **37**, 1079-1104.
29. A. A. Zadpoor and J. Malda, *Annals of Biomedical Engineering*, 2017, **45**, 1-11.
30. C. P. de Jonge, H. M. A. Kolken and A. A. Zadpoor, *Materials*, 2019, **12**, 635.
31. R. Wauthle, S. M. Ahmadi, S. A. Yavari, M. Mulier, A. A. Zadpoor, H. Weinans, J. Van Humbeeck, J.-P. Kruth and J. Schrooten, *Materials Science and Engineering: C*, 2015, **54**, 94-100.
32. W. Peng, L. Xu, J. You, L. Fang and Q. Zhang, *Biomedical engineering online*, 2016, **15**, 85.
33. A. A. Zadpoor, *Biomaterials science*, 2015, **3**, 231-245.
34. Y. Wang, L. Zhang, S. Daynes, H. Zhang, S. Feih and M. Y. Wang, *Materials & Design*, 2018, **142**, 114-123.
35. E. Onal, J. Frith, M. Jurg, X. Wu and A. Molotnikov, *Metals*, 2018, **8**, 200.
36. I. Maskery, N. T. Aboulkhair, A. O. Aremu, C. J. Tuck, I. A. Ashcroft, R. D. Wildman and R. J. M. Hague, *Materials Science and Engineering: A*, 2016, **670**, 264-274.
37. G. H. Loh, E. Pei, D. Harrison and M. D. Monzón, *Additive Manufacturing*, 2018, **23**, 34-44.
38. M. Fousová, D. Vojtěch, J. Kubásek, E. Jablonská and J. Fojt, *Journal of the Mechanical Behavior of Biomedical Materials*, 2017, **69**, 368-376.
39. S. Y. Choy, C.-N. Sun, K. F. Leong and J. Wei, *Materials & Design*, 2017.
40. D. S. J. Al-Saedi, S. H. Masood, M. Faizan-Ur-Rab, A. Alomarah and P. Ponnusamy, *Materials & Design*, 2018, **144**, 32-44.
41. M. Afshar, A. P. Anaraki, H. Montazerian and J. Kadkhodapour, *Journal of the Mechanical Behavior of Biomedical Materials*, 2016, **62**, 481-494.
42. J.-Y. Rho, L. Kuhn-Spearing and P. Zioupos, *Medical Engineering & Physics*, 1998, **20**, 92-102.
43. C. Han, Y. Li, Q. Wang, S. Wen, Q. Wei, C. Yan, L. Hao, J. Liu and Y. Shi, *Journal of the Mechanical Behavior of Biomedical Materials*, 2018, **80**, 119-127.
44. S. Li, S. Zhao, W. Hou, C. Teng, Y. Hao, Y. Li, R. Yang and R. D. K. Misra, *Advanced Engineering Materials*, 2016, **18**, 34-38.
45. R. Hedayati, S. Ahmadi, K. Lietaert, B. Pouran, Y. Li, H. Weinans, C. Rans and A. Zadpoor, *Journal of the mechanical behavior of biomedical materials*, 2018.
46. L. J. Gibson and M. F. Ashby, in *Cellular Solids: Structure and Properties*, eds. L. J. Gibson and M. F. Ashby, Cambridge University Press, Cambridge, 2 edn., 1997, DOI: DOI: 10.1017/CBO9781139878326.013, pp. 429-452.
47. M. F. Ashby, *Philosophical Transactions: Mathematical, Physical and Engineering Sciences*, 2006, **364**, 15-30.
48. K. Genovese, S. Leeflang and A. A. Zadpoor, *Journal of the Mechanical Behavior of Biomedical Materials*, 2017, **69**, 327-341.
49. M. Smith, Z. Guan and W. J. Cantwell, *International Journal of Mechanical Sciences*, 2013, **67**, 28-41.
50. S. M. Ahmadi, G. Campoli, S. Amin Yavari, B. Sajadi, R. Wauthle, J. Schrooten, H. Weinans and A. A. Zadpoor, *Journal of the Mechanical Behavior of Biomedical Materials*, 2014, **34**, 106-115.
51. Ó. L. Rodríguez-Montaño, C. J. Cortés-Rodríguez, A. E. Uva, M. Fiorentino, M. Gattullo, G. Monno and A. Boccaccio, *Journal of the Mechanical Behavior of Biomedical Materials*, 2018, **83**, 28-45.
52. R. Hedayati, M. Sadighi, M. Mohammadi-Aghdam and A. A. Zadpoor, *Materials Science and Engineering: C*, 2016, **60**, 163-183.
53. R. Hedayati, M. Sadighi, M. Mohammadi-Aghdam and A. A. Zadpoor, *International Journal of Mechanical Sciences*, 2016, **106**, 19-38.
54. S. Babaee, B. H. Jahromi, A. Ajdari, H. Nayeb-Hashemi and A. Vaziri, *Acta Materialia*, 2012, **60**, 2873-2885.
55. O. L. A. Harrysson, O. Cansizoglu, D. J. Marcellin-Little, D. R. Cormier and H. A. West, *Materials Science and Engineering: C*, 2008, **28**, 366-373.
56. R. Hedayati, H. Hosseini-Toudeshky, M. Sadighi, M. Mohammadi-Aghdam and A. A. Zadpoor, *International Journal of Fatigue*, 2016, **84**, 67-79.

57. S. Arabnejad, R. Burnett Johnston, J. A. Pura, B. Singh, M. Tanzer and D. Pasini, *Acta Biomaterialia*, 2016, **30**, 345-356.
58. 3D Systems, 2017, Direct Metal Printers: Metal Additive Manufacturing with the DMP printer series
59. N. Guo and M. C. Leu, *Frontiers of Mechanical Engineering*, 2013, **8**, 215-243.
60. 3D Systems, 2017, LaserForm® Ti Gr1 (A)
61. 2017, Standard Specification for Unalloyed Titanium, for Surgical Implant Applications (UNS R50250, UNS R50400, UNS R50550, UNS R50700)
62. ASTM, 2015, B265 - 15: Standard Specification for Titanium and Titanium Alloy Strip, Sheet, and Plate
63. ASTM, 2013, B348-13: Standard Specification for Titanium and Titanium Alloy Bars and Billets
64. ISO, 2018, 5832-2: Implants for surgery -- Metallic materials -- Part 2: Unalloyed titanium
65. ISO, 1996, 13782: Implants for surgery -- Metallic materials -- Unalloyed tantalum for surgical implant applications
66. Werkstoff, 2018, Werkstoff Nr. 37025
67. Sawbones, *Available from: http://live.sawbones.com/wp-content/uploads/2017/04/FINAL_Biomechanical_Catalog.pdf*, 2017.
68. W. G. Paprosky, P. G. Perona and J. M. Lawrence, *The Journal of Arthroplasty*, 1994, **9**, 33-44.
69. M. Doube, M. M. Kłosowski, I. Arganda-Carreras, F. P. Cordelières, R. P. Dougherty, J. S. Jackson, B. Schmid, J. R. Hutchinson and S. J. Shefelbine, *Bone*, 2010, **47**, 1076-1079.
70. ISO, 2011, 13314:2011 Mechanical Testing of Metals—Ductility Testing—Compression Test for Porous and Cellular Metals
71. S. Kalidindi, A. Abusafieh and E. El-Danaf, *Experimental mechanics*, 1997, **37**, 210-215.
72. H. M. Kolken, S. Janbaz, S. M. Leeflang, K. Lietaert, H. H. Weinans and A. A. Zadpoor, *Materials Horizons*, 2018, **5**, 28-35.
73. IBM, *Journal*, 2017.
74. J. Jaccard and J. Jaccard, *Interaction effects in factorial analysis of variance*, Sage, 1998.
75. R. Hedayati, S. Janbaz, M. Sadighi, M. Mohammadi-Aghdam and A. A. Zadpoor, *Journal of the Mechanical Behavior of Biomedical Materials*, 2017, **65**, 831-841.
76. H. Attar, L. Löber, A. Funk, M. Calin, L. C. Zhang, K. G. Prashanth, S. Scudino, Y. S. Zhang and J. Eckert, *Materials Science and Engineering: A*, 2015, **625**, 350-356.
77. F. Li, J. Li, T. Huang, H. Kou and L. Zhou, *Journal of the Mechanical Behavior of Biomedical Materials*, 2017, **65**, 814-823.
78. F. A. Shah, M. Trobos, P. Thomsen and A. Palmquist, *Materials Science and Engineering: C*, 2016, **62**, 960-966.
79. X. P. Li, J. Van Humbeeck and J. P. Kruth, *Materials & Design*, 2017, **116**, 352-358.
80. L. Mullen, R. C. Stamp, P. Fox, E. Jones, C. Ngo and C. J. Sutcliffe, *Journal of Biomedical Materials Research Part B: Applied Biomaterials*, 2010, **92**, 178-188.
81. S. L. Sing, W. Y. Yeong, F. E. Wiria and B. Y. Tay, *Experimental Mechanics*, 2016, **56**, 735-748.
82. A. Barbas, A.-S. Bonnet, P. Lipinski, R. Pesci and G. Dubois, *Journal of the mechanical behavior of biomedical materials*, 2012, **9**, 34-44.
83. V. S. Deshpande, M. F. Ashby and N. A. Fleck, *Acta Materialia*, 2001, **49**, 1035-1040.
84. A. A. Zadpoor, *J Mech Behav Biomed Mater*, 2017, **70**, 1-6.
85. S. Amin Yavari, R. Wauthle, J. van der Stok, A. C. Riemslag, M. Janssen, M. Mulier, J. P. Kruth, J. Schrooten, H. Weinans and A. A. Zadpoor, *Materials Science and Engineering: C*, 2013, **33**, 4849-4858.
86. S. Amin Yavari, S. M. Ahmadi, J. van der Stok, R. Wauthle, A. C. Riemslag, M. Janssen, J. Schrooten, H. Weinans and A. A. Zadpoor, *Journal of the Mechanical Behavior of Biomedical Materials*, 2014, **36**, 109-119.
87. R. Hedayati, M. Sadighi, M. Mohammadi-Aghdam and H. Hosseini-Toudeshky, *Journal of Biomedical Materials Research Part B: Applied Biomaterials*, 2017.
88. G. N. Greaves, A. Greer, R. Lakes and T. Rouxel, *Nature materials*, 2011, **10**, 823.

89. X. Y. Cheng, S. J. Li, L. E. Murr, Z. B. Zhang, Y. L. Hao, R. Yang, F. Medina and R. B. Wicker, *Journal of the Mechanical Behavior of Biomedical Materials*, 2012, **16**, 153-162.
90. B. Gorny, T. Niendorf, J. Lackmann, M. Thoene, T. Troester and H. J. Maier, *Materials Science and Engineering: A*, 2011, **528**, 7962-7967.
91. T. Niendorf, F. Brenne and M. Schaper, *Metallurgical and Materials Transactions B*, 2014, **45**, 1181-1185.
92. L. Xiao and W. Song, *International Journal of Impact Engineering*, 2018, **111**, 255-272.
93. A. Acciaioli, G. Lionello and M. Baleani, *Materials (Basel, Switzerland)*, 2018, **11**, 751.
94. S. Amin Yavari, S. M. Ahmadi, R. Wauthle, B. Pouran, J. Schrooten, H. Weinans and A. A. Zadpoor, *Journal of the Mechanical Behavior of Biomedical Materials*, 2015, **43**, 91-100.
95. R. Wauthle, B. Vrancken, B. Beynaerts, K. Jorissen, J. Schrooten, J.-P. Kruth and J. Van Humbeeck, *Additive Manufacturing*, 2015, **5**, 77-84.
96. L. Liu, P. Kamm, F. García-Moreno, J. Banhart and D. Pasini, *Journal of the Mechanics and Physics of Solids*, 2017, **107**, 160-184.
97. V. Weißmann, R. Bader, H. Hansmann and N. Laufer, *Materials & Design*, 2016, **95**, 188-197.
98. H. V. Wang, S. R. Johnston and D. W. Rosen, 2006.
99. X. Wang, S. Xu, S. Zhou, W. Xu, M. Leary, P. Choong, M. Qian, M. Brandt and Y. M. Xie, *Biomaterials*, 2016, **83**, 127-141.
100. P. S. D. Patel, D. E. T. Shepherd and D. W. L. Hukins, *BMC Musculoskeletal Disorders*, 2008, **9**, 137.
101. C. West and J. C. Fryman, 2008.
102. M. J. Nine, D. Choudhury, A. C. Hee, R. Mootanah and N. A. A. Osman, *Materials*, 2014, **7**, 980-1016.
103. M. Baauw, G. G. van Hellemondt and M. Spruit, *Orthopedics*, 2017, **40**, e195-e198.
104. J. de Krijger, C. Rans, B. Van Hooreweder, K. Lietaert, B. Pouran and A. A. Zadpoor, *Journal of the Mechanical Behavior of Biomedical Materials*, 2017, **70**, 7-16.
105. C. M. Bidan, F. M. Wang and J. W. C. Dunlop, *Computer Methods in Biomechanics and Biomedical Engineering*, 2013, **16**, 1056-1070.
106. Y. Li, H. Jahr, K. Lietaert, P. Pavanram, A. Yilmaz, L. I. Fockaert, M. A. Leeflang, B. Pouran, Y. Gonzalez-Garcia, H. Weinans, J. M. C. Mol, J. Zhou and A. A. Zadpoor, *Acta Biomaterialia*, 2018, **77**, 380-393.
107. B. Song, S. Dong, Q. Liu, H. Liao and C. Coddet, *Materials & Design (1980-2015)*, 2014, **54**, 727-733.

8
Appendix

Table A1 The designed dimensions of the non-auxetic meta-biomaterials.
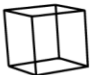
Type	Porosity [%] CAD	Strut thickness [μm]	Strut length [mm]	Sample size [mm] length	width	height
C	80	1539	4.700	23.50	23.50	23.50
	85	1314	4.730	23.65	23.65	23.65
	90	1074	4.800	24.00	24.00	24.00
	95	755	4.890	24.45	24.45	24.45
	98	487	4.900	24.50	24.50	24.50
TC	80	1299	1.988	24.00	24.00	24.00
	85	1025	1.988	24.00	24.00	24.00
	90	803	2.009	24.25	24.25	24.25
	95	561	2.030	24.50	24.50	24.50
	98	336	2.050	24.75	24.75	24.75
TCO	80	1299	38.85	24.00	24.00	24.00
	85	1025	26.63	24.50	24.50	24.50
	90	803	18.53	24.50	24.50	24.50
	95	561	7.32	24.50	24.50	24.50
	98	336	1.37	24.50	24.50	24.50
RD-YZ	80	745	1.254	16.91	16.91	24.00
	85	632	1.280	16.91	16.91	24.00
	90	506	1.280	16.91	16.91	24.00
	95	371	1.280	17.27	17.27	24.50
	98	228	1.280	16.91	16.91	24.00
RD-X	80	745	1.254	16.91	24.00	16.91
	85	632	1.280	16.91	24.00	16.91
	90	506	1.280	16.91	24.00	16.91
	95	371	1.280	17.27	24.50	17.27
	98	228	1.280	16.91	24.00	16.91
D	80	1036	1.748	24.00	24.00	24.00
	85	895	1.748	24.00	24.00	24.00
	90	717	1.748	24.00	24.00	24.00
	95	507	1.785	24.50	24.50	24.50
	98	325	1.785	24.50	24.50	24.50
BCC	80	1037	4.157	24.00	24.00	24.00
	85	883	4.157	24.00	24.00	24.00
	90	719	4.200	24.25	24.25	24.25
	95	504	4.244	24.50	24.50	24.50
	98	314	4.244	24.50	24.50	24.50

Type			Porosity [%]					Strut thickness [μm]			Pore Size [μm]	
			CAD	DW	std.	μCT	std.	CAD	μCT	std.	μCT	std.
BCC		MIN	90	91.72	0.30	91.63	0.21	450	424	8.77	1734	121
		MAX	98	97.81	0.02	96.40	0.57	200	252	21.92	1718	2.30
D		MIN	90	90.44	0.20	89.50	0.49	450	453	14.88	1633	18.7
		MAX	98	96.86	0.20	95.47	0.12	200	281	4.32	1819	4.88
RD		MIN	90	89.38	0.30	89.93	0.45	320	357	11.44	1544	0.50
		MAX	96	93.85	0.10	94.10	0.36	200	294	2.97	1646	5.47

Table A2 Morphological characteristics of the uniform porous acetabular.

Table A3 Morphological characteristics of the functionally graded acetabular implants.

Type			Porosity [%]	Strut thickness [μm]
			CAD	CAD
BCC		FG	90	450
			95	310
			98	200
D		FG	90	450
			95	310
			98	200
RD		FG	90	320
			93	260
			96	200
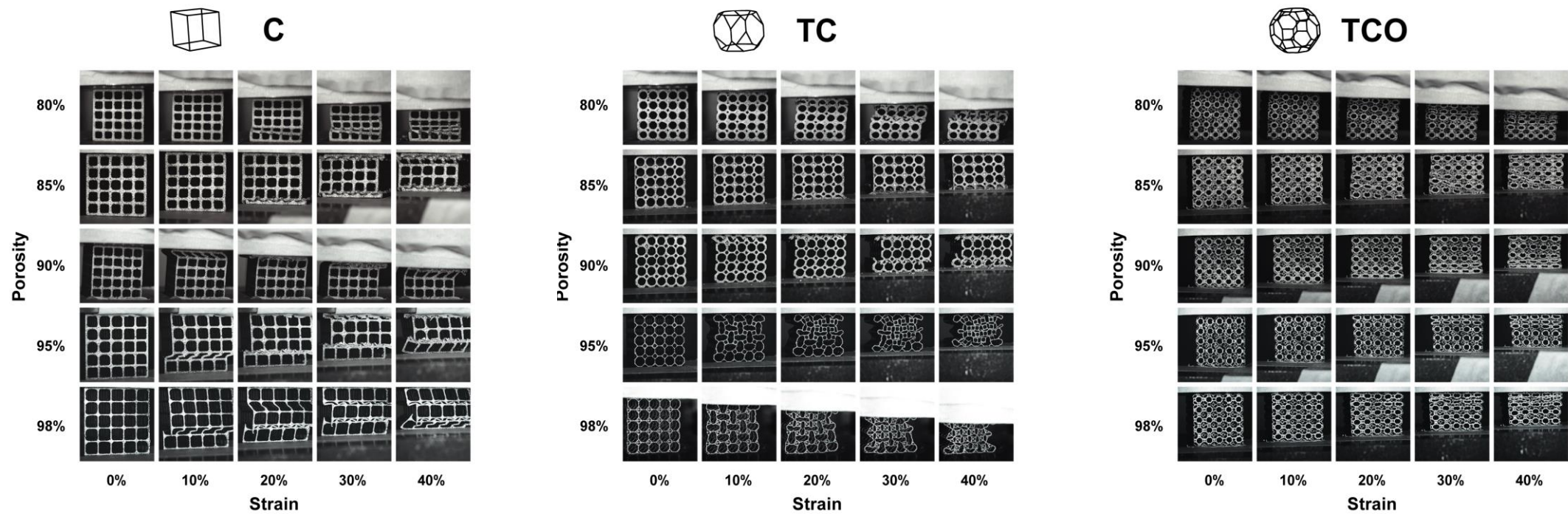
Figure A1: Deformation pattern of the non-auxetic meta-biomaterials.
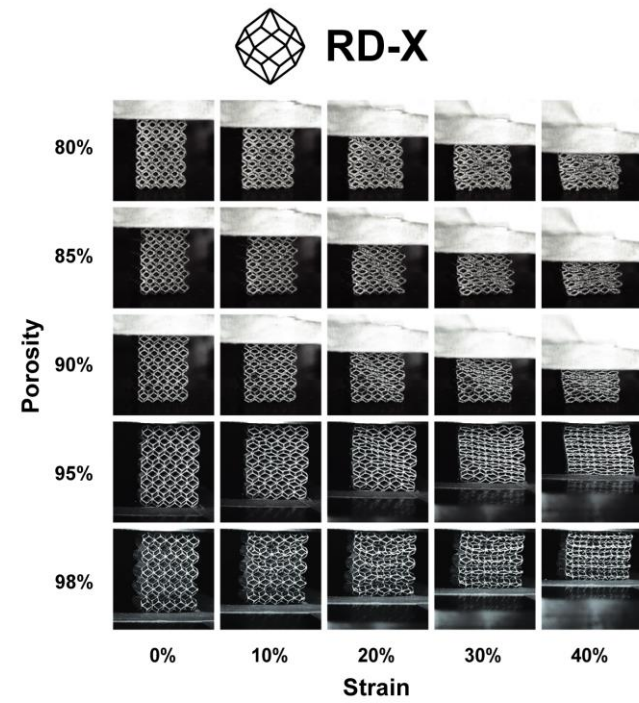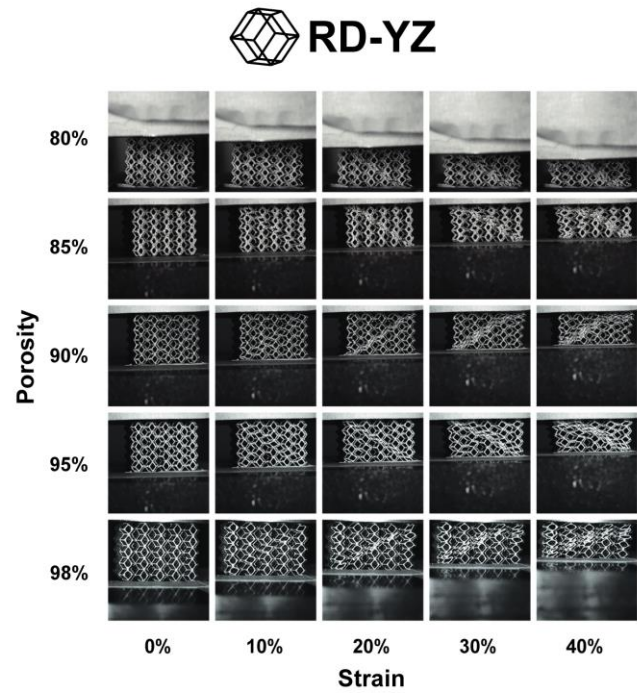
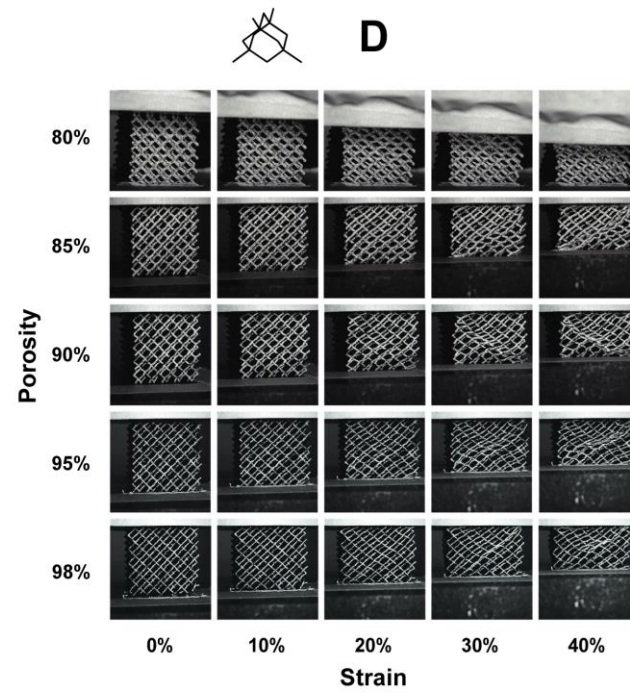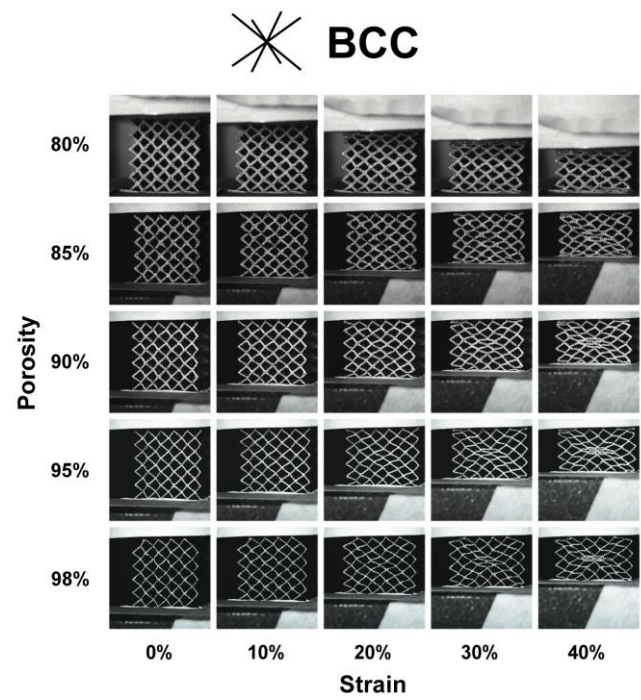**Figure A1 (continued): Deformation pattern of the non-auxetic meta-biomaterials.**

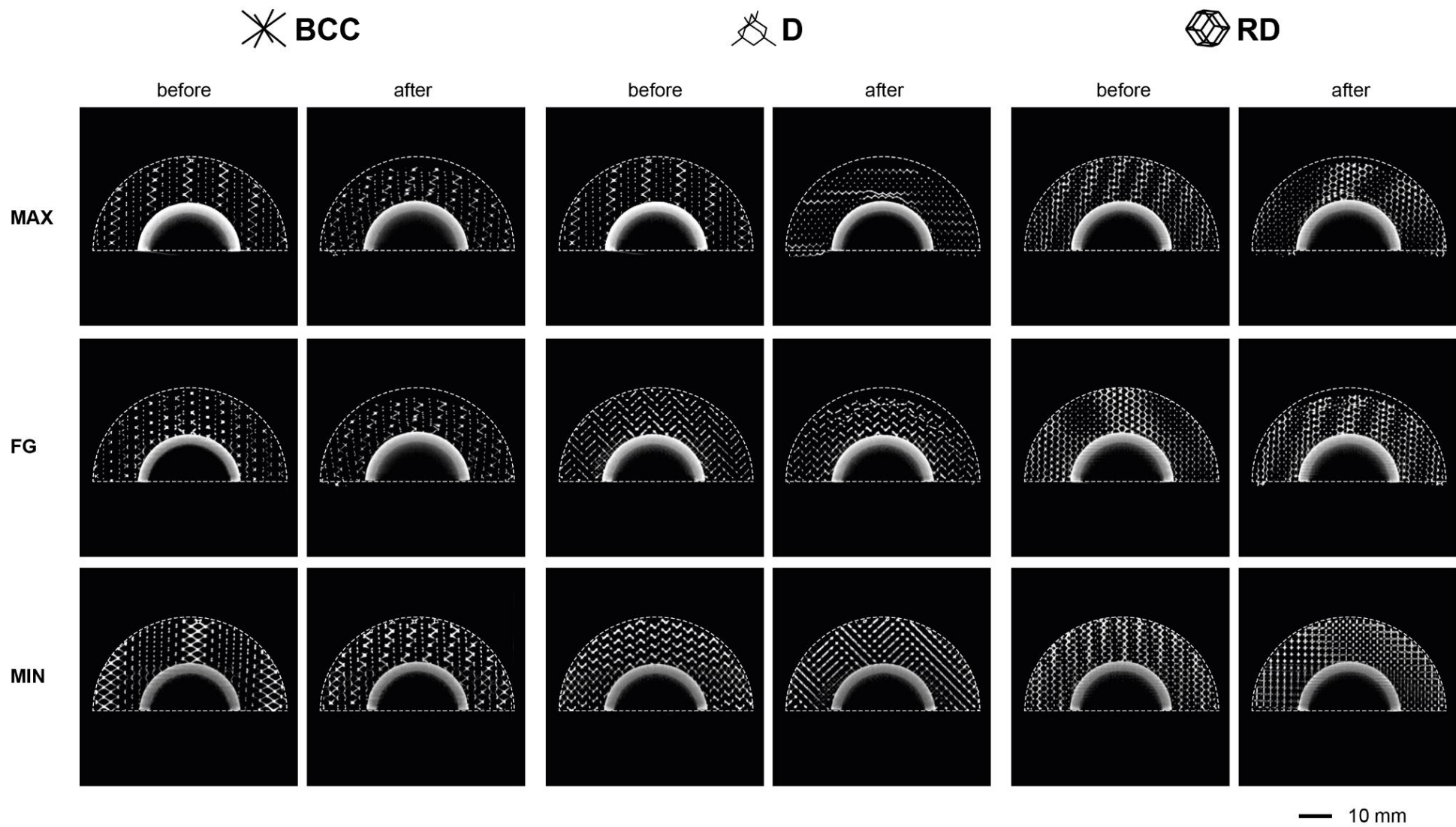**Figure A1 (continued): Deformation pattern of the non-auxetic meta-biomaterials.**

Figure A2: CT Scans of the acetabular implants before and after compression.
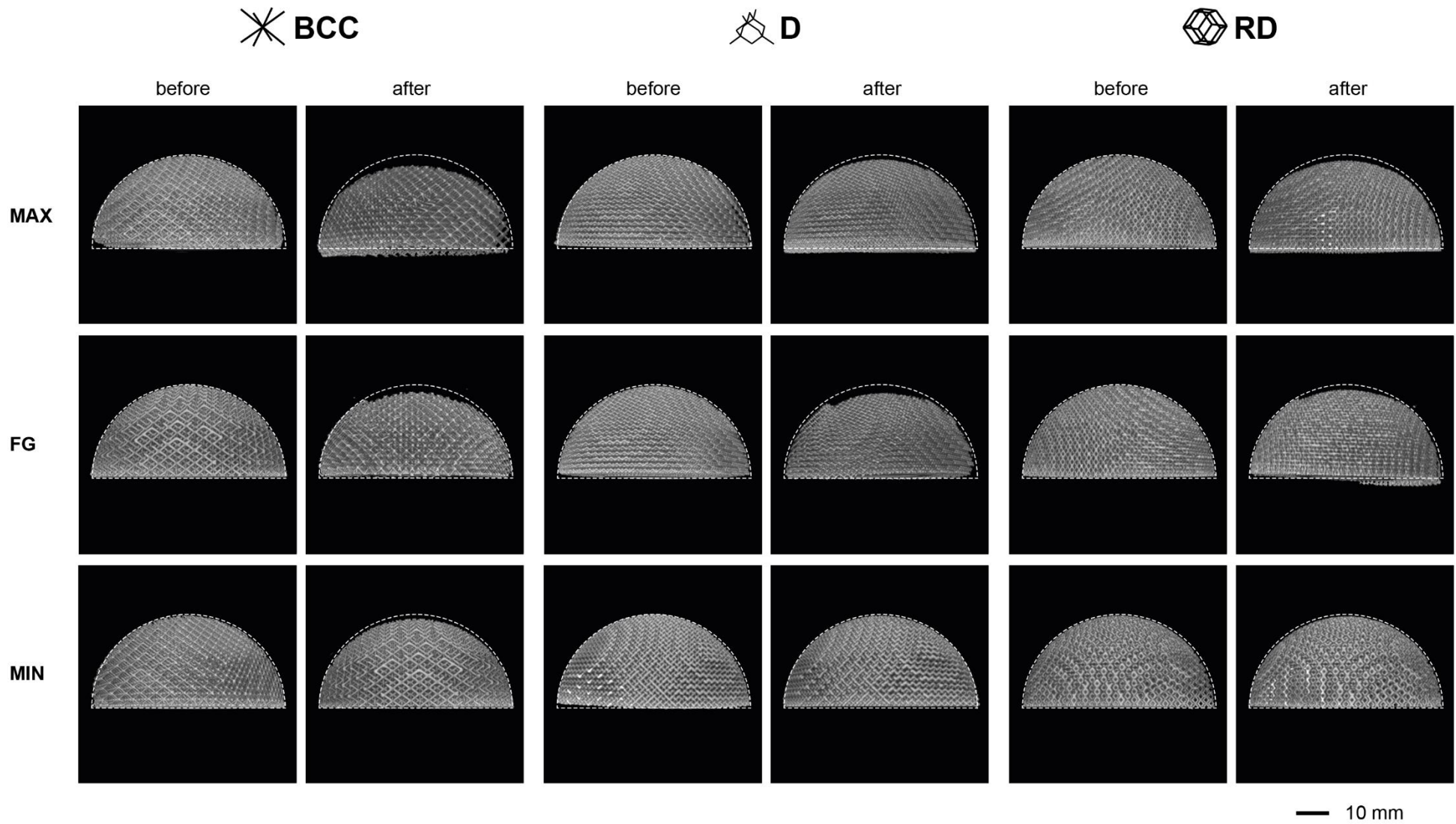
Figure A3: 3D representations of the acetabular implants before and after compression.
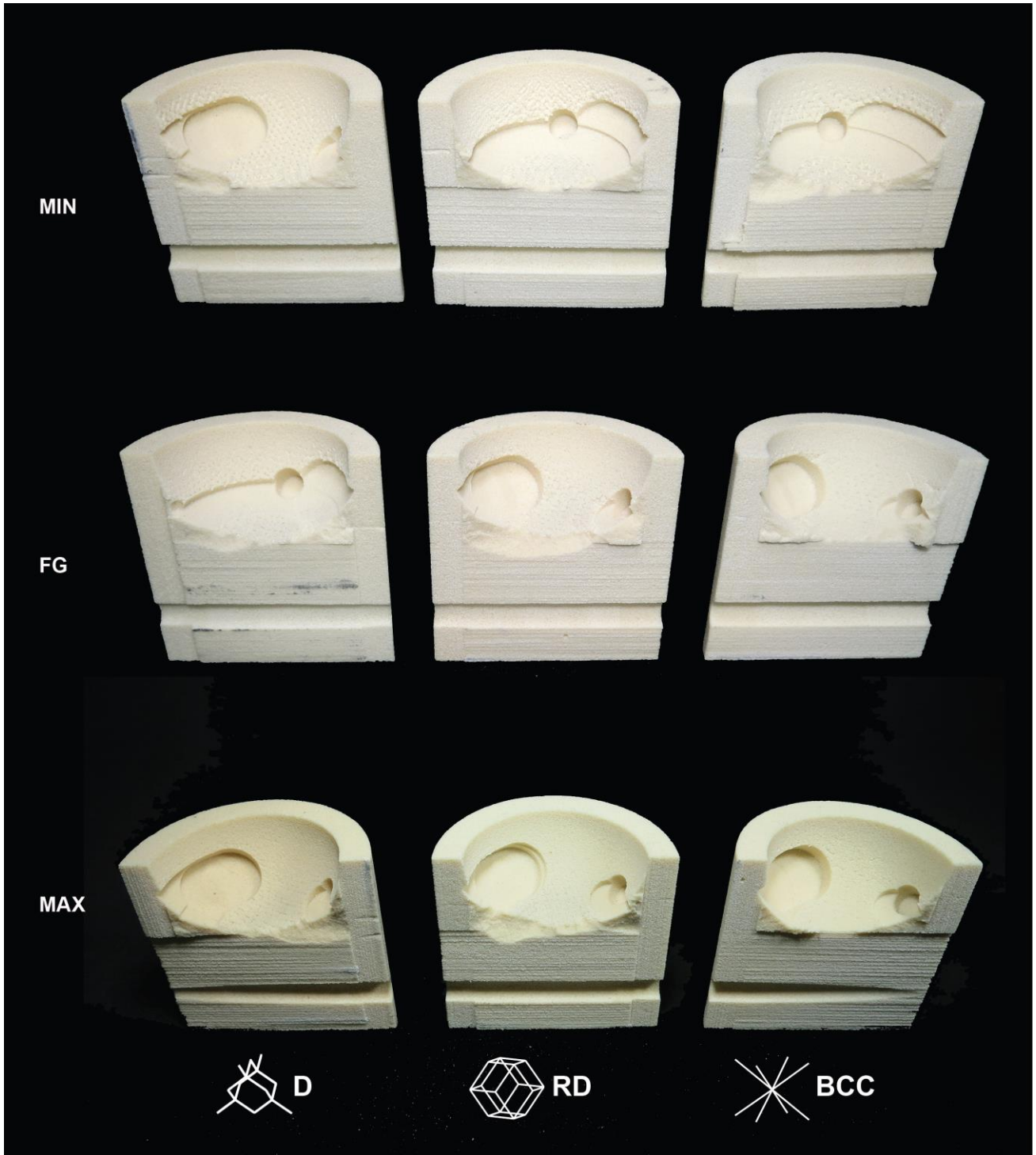
Figure A4: The moulds after being cut in half. These moulds were compressed by acetabular implants based on a diamond unit cell. (a) MIN design (90%), (b) FG design, (c) MAX design (96/98%).